Univerzita Karlova v Praze

Matematicko-fyzikální fakulta

DIPLOMOVÁ PRÁCE

Bc. Kristína Václavová

Mikrostruktura a mechanické vlastnosti ultrajemnozrnných slitin titanu

Katedra fyziky materiálů

Vedoucí diplomové práce: PhDr. RNDr. Josef Stráský, Ph.D.

Studijní program: Fyzika

Studijní obor: Fyzika kondenzovaných soustav a materiálů

Praha 2015

Charles University in Prague

Faculty of Mathematics and Physics

MASTER THESIS

Bc. Kristína Václavová

Microstructure and mechanical properties of ultra-fine grained titanium alloys

Department of Physics of Materials

Supervisor of the master thesis: PhDr. RNDr. Josef Stráský, Ph.D.

Study programme: Physics

Specialization: Physics of condensed matter and materials

Prague 2015

Acknowledgement

First of all, I would like to express my appreciation above all to my supervisor PhDr. RNDr. Josef Stráský, Ph.D. for consultation, giving advice and for help during writing my thesis. My sincere thanks are also extended to RNDr. Jitka Stráská, Ph.D. for SEM observation and EBSD mapping, to RNDr. Petr Harcuba and Assoc. Prof. Miloš Janeček CSc. for their consultations and for technical advice. My gratitude also goes to Ing. Jana Kálalová for assistance during working in a chemical laboratory, to RNDr. Jan Čapek for helping in evaluation of the EBSD images and to Assoc. Prof. Jakub Čížek, Ph.D. for providing the positron annihilation spectroscopy measurements.

I declare that I carried out this master thesis independently, and only with the cited sources, literature and other professional sources.

I understand that my work relates to the rights and obligations under the Act No. 121/2000 Coll., the Copyright Act, as amended, in particular the fact that the Charles University in Prague has the right to conclude a license agreement on the use of this work as a school work pursuant to Section 60 paragraph 1 of the Copyright Act.

In Prague 06/05/2015

Bc. Kristína Václavová

Název práce: Mikrostruktura a mechanické vlastnosti ultrajemnozrnných slitin titanu

Autor: Bc. Kristína Václavová

Katedra / Ústav: Katedra fyziky materiálů

Vedoucí diplomové práce: PhDr. RNDr. Josef Stráský, Ph.D.

Abstrakt: Metastabilní β-slitiny titanu Ti-15Mo a Ti-6,8Mo-4,5Fe-1,5Al (TIMETAL LCB) byly připraveny metodou torze za vysokého tlaku (HPT), která patří mezi metody intenzivní plastické deformace (SPD). Mikrotvrdost slitin Ti-15Mo a TIMETAL LCB se zvyšuje s rostoucí vloženou deformací – tedy se zvyšujícím se počtem otáček HPT a také s rostoucí vzdáleností od středu vzorku. Nejvyšší hodnoty mikrotvrdosti po deformaci HPT výrazně převyšují mikrotvrdost dvoufázového α + β materiálu po tepelném zpracování. Deformovaná mikrostruktura byla studována rastrovací elektronovou mikroskopií a difrakcí zpětně odražených elektronů (EBSD). Výrazné dvojčatění bylo pozorováno u obou studovaných slitin. Mechanismus vícenásobného dvojčatění výrazně přispívá k fragmentaci zrn a tedy ke zjemnění mikrostruktury. Struktura defektů ve slitině Ti-15Mo byla studována pomocí pozitronové anihilační spektroskopie. Jedinými defekty detekovanými pozitronovou anihilační spektroskopií jsou dislokace. Hustota dislokací se zvyšuje s počtem HPT otáček a s rostoucí vzdáleností od středu vzorku. Nárůst hustoty dislokací je podstatným zdrojem nárůstu mikrotvrdosti slitiny Ti-15Mo. Vliv HPT deformace na fázové přeměny slitiny Ti-15Mo byl zkoumán pomocí diferenční skenovací kalorimetrie. Deformovaná struktura zásadním způsobem ovlivňuje fázové transformace v materiálu. Přesné vysvětlení vlivu ultra-jemnozrnné mikrostruktury na fázové transformace však vyžaduje další podrobné zkoumání.

Klíčová slova: ultrajemnozrnný materiál, slitiny titanu, mikrostruktura, mikrotvrdost, difrakce zpětně odražených elektronů, struktura defektů, fázové transformace

Title: Microstructure and mechanical properties of ultra-fine grained titanium alloys

Author: Bc. Kristína Václavová

Department / Institute: Department of Physics of Materials

Supervisor of the master thesis: PhDr. RNDr. Josef Stráský, Ph.D.

Abstract: Metastable β-Ti alloys Ti-15Mo and Ti-6.8Mo-4.5Fe-1.5Al (TIMETAL LCB) were subjected to severe plastic deformation by high pressure torsion. Microhardness of Ti-15Mo and TIMETAL LCB alloys increases with increasing inserted deformation, i.e. with increasing number of HPT rotations and also with increasing distance from the centre of the sample. The highest microhardness after HPT exceeds significantly the microhardness of two-phase α + β heat-treated material. Increasingly deformed microstructure was also demonstrated by scanning electron microscopy and by electron back-scattered diffraction (EBSD). Significant twinning was observed in both studied alloys. Mechanism of multiple twinning contributes notably to the fragmentation of grains and thus to the refinement of the microstructure. Defect structure in Ti-15Mo alloy was studied by positron annihilation spectroscopy. It was proved that dislocations are the only detectable defects in the material by positron annihilation spectroscopy and that dislocation density increases with the number of HPT revolution and with the distance from the centre on the specimen. The increase in the dislocation density is one of the causes of the increased microhardness of Ti-15Mo alloy. The effect of the HPT deformation on the phase transformations was examined by differential scanning calorimetry. Deformed microstructure significantly influences phase transformations in the material. The precise explanation of the effect of the ultra-fine grained microstructure on the phase transformations however requires detailed further investigations.

Keywords: ultra-fine grained materials, Ti alloys, microstructure, microhardness, electron back-scattered diffraction, defect structure, phase transformations

Contents

1. Introduction

Titanium was discovered in Cornwall, Great Britain, by William Gregor in 1791; however the first commercial production of titanium as a metal was only in 1948. Titanium is named after the Titans from the Greek mythology. It is not actually a rare substance as it ranks as the ninth most plentiful element and the fourth most abundant structural metal in the Earth's crust, but its isolation from ores is extremely hard [1].

Titanium and titanium alloys are increasingly used in many applications due to their excellent properties: extreme corrosion resistance, relatively high strength, sufficient biocompatibility, low density and moderate elastic modulus among others. Today, aircraft industry is the prime consumer of titanium and its alloys, but other markets such as architecture, chemical processing, medicine, power generation, marine and offshore, sports and leisure are gaining increased acceptance [1]. The only downside of utilization of the above-mentioned areas is the high price of the material when compared to steels or aluminium.

In the last few decades, the importance of β-titanium alloys increased significantly. Examples of metastable β-titanium alloys are such as Beta C (Ti-3Al-8V-6Cr-4Mo-4Zr), Beta CEZ (Ti-5Al-2Sn-4Zr-4Mo-2Cr-1Fe), Ti-15-3-3 (Ti-15V-3Cr-3Sn-3Al), Beta 21s (Ti-15Mo-3Al-3Nb-0.2Si), TIMETAL LCB - low-cost beta (Ti-6.8Mo-4.5Fe-1.5Al) or a binary alloy Ti-15Mo [2]. Advanced β-Ti alloys have been extensively used in aircraft manufacturing since 1980s and their usage is still growing [1]. The unique properties of these materials include high strength, excellent corrosion resistance and low density in comparison with steels. High strength is usually achieved by advanced thermo-mechanical treatment involving precipitation of α-phase particles.

In this thesis, two alloys are studied: Ti-15Mo alloy and TIMETAL LCB (Ti-6,8Mo-4,5Fe-1,5Al). Ti-15Mo alloy is relatively simple binary alloy; however, it exhibits good mechanical properties and the absence of toxic elements (vanadium, etc.). TIMETAL LCB (low-cost beta) alloy is characterized by lower production costs due to the partial replacement of the relatively expensive β-stabilizing dopants such as vanadium or molybdenum by iron. This alloy is also used in the automotive industry (e.g. for the production of suspension springs). It is known that thanks to

high strength, low weight and low elastic modulus when compared to steels, up to 60% weight of suspension springs can be saved.

The investigated β-Ti alloys were subjected to severe plastic deformation (SPD) by high pressure torsion (HPT) technique. SPD methods allow inserting very large deformation to the material without changing the shape of samples. Thus prepared material is ultra-fine grained with better mechanical and physical properties. Mechanical properties were studied by microhardness measurements, the microstructure evolution was examined by scanning electron microscopy and electron backscatter diffraction (EBSD). The defect structure was observed by positron annihilation spectroscopy (PAS) and phase transformations by differential scanning calorimetry (DSC).

This master thesis is divided into eight chapters. Chapter 2 characterizes the fundamental properties of titanium and its alloys. In this chapter, various phases and phase transformations in Ti alloys are discussed. Chapter 3 provides information about fundamental properties, preparation and applications of ultra-fine grained materials. This chapter also describes the SPD technique used in this thesis – the high pressure torsion – for preparing ultra-fine grained material. Chapter 4 includes description the experimental materials. Chapter 5 describes the experimental methods used for alloys characterization and chapter 6 summarizes the aims and objectives of the present thesis. The most voluminous chapter 7 presents the results and discussion. Finally, chapter 8 concludes the results of the study and introduces the possibilities of future investigations.

# 2.	Titanium and its alloys

Titanium has atomic number 22 and belongs to Group 4 of the periodic table of elements. It has a silver colour and with a density of 4.51 g/cm^3 is the heaviest light metal [1]. In nature, it occurs in five isotopes, ^{46}Ti through ^{50}Ti, where the ^{48}Ti is the most abundant structural metal [3]. Moreover, naturally it occurs in bonding with other elements. The most important mineral sources are rutile (TiO_2) and ilmenite ($FeTiO_3$). Titanium is produced from these two ores by the Kroll process. The chemical reactions of process can be written as follows [4]:

$$TiO_2 + 2Cl_2 + 2C \rightarrow TiCl_4 + 2CO \tag{2.1}$$

$$TiCl_4 + 2Mg \rightarrow 2MgCl_2 + Ti \tag{2.2}$$

The first step of the Kroll process is the preparation of the titanium tetrachloride; afterwards, the liquid $TiCl_4$ is introduced to the liquid Mg. The reaction products are so-called "titanium sponge" and liquid $MgCl_2$, most of which can be drained out of the reaction chamber [5].

The next stage of the manufacturing is crushing and sizing of the sponge to produce granules of metallic titanium. The bulk material of the titanium is prepared from these granules. The preparation should take place in vacuum or protective inert atmosphere because titanium is extremely reactive with oxygen and nitrogen [2].

## 2.1.	Crystallography

Titanium is a polymorphic material which means that it occurs in more than one phase. Phases should be divided into equilibrium (stable) and non-equilibrium (unstable or metastable) phases. The equilibrium phase is determined by the lowest Gibbs free enthalpy (G), under the given circumstances. However, there are other configurations that correspond to the local minimum of Gibbs free enthalpy, but not to the global minimum. Such configurations are called metastable phases and can be formed either by displacive transformation (shearing, shuffling) or diffusional transformation when a high cooling or heating rate is chosen. Under favourable conditions and after an appropriate amount of time the metastable phases can be transformed to the stable ones.

2.1.1. Equilibrium phases

Pure titanium crystallizes in a hexagonal close-packed (HCP) stable structure at room temperature and normal pressure which is known as α-phase. The space group of this phase is *P6₃mmc*. The unit cell of α-phase is shown in Fig. 2.1. with the lattice parameters: $a = 2.95 \cdot 10^{-10}$ m and $c = 4.68 \cdot 10^{-10}$ m. The c/a ratio is *1.586* thus it is slightly smaller than the ideal ratio (1.633).

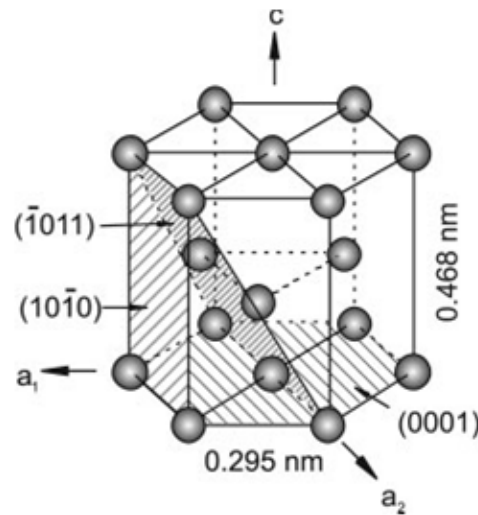
Fig. 2.1. Hexagonal close-packed cell of α phase [2]

In case of pure titanium, the β-transus temperature is *1155 K* which means that material transforms from the α-phase to the body-centered cubic (BCC) phase, which is known as β-phase, when heated above this temperature. At high temperatures β-phase is a stable one. The lattice parameter of the β-phase is $3.32 \cdot 10^{-10}$ m (see also Fig 2.2.) and with two atoms per unit cell the BCC structure has the space group *Im3m*. The more opened structure of the BCC structure is able to accommodate higher vibrational entropy; therefore, it is more stable at higher temperatures than the HCP structure of the α-phase.

In case of titanium alloys, β-transition temperature strongly depends on the content of impurity and alloying elements. Impurities and alloying elements in titanium alloys are divided into three groups, depending on how they affect the phase-transition temperature:

1) α-stabilizing elements (e.g. Al, O, N, C)

2) β-stabilizing elements (e.g. V, Mo, Fe, Nb, Cr)

3) neutral (e.g. Zr, Sn)

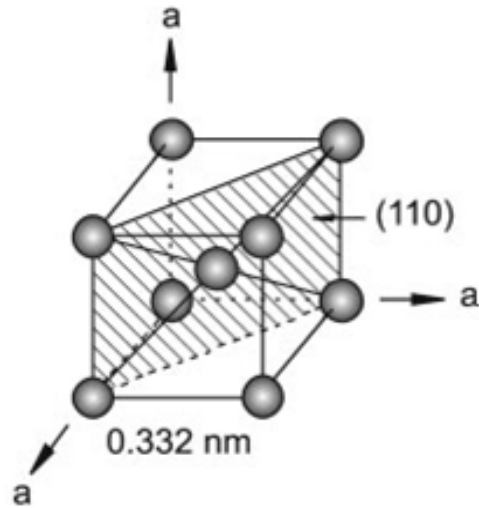Fig. 2.2. Body-centered cubic cell of the β-phase [2]

α-stabilizing elements increase the β-transus temperature and extend the zone of the stability of the α-phase. Conversely, the β-stabilizing elements reduce β-transus temperature and thereby effectively widen the range of the β-phase. These alloying elements can be further divided into β-isomorphous and β-eutectoid elements depending on their solubility in β-phase. The effect of these elements on phase diagrams is schematically shown in Fig. 2.3.

The effect of individual stabilizers in titanium alloys may be expressed by the so-called molybdenum equivalency depending on the amount of each addition needed to lower the martensitic decomposition of β-phase into α-phase below room temperature [6]:

$$[Mo]_{eq.} = [Mo] + 0.67\,[V] + 0.44\,[W] + 0.28\,[Nb] + 0.22\,[Ta] + 2.9\,[Fe] + 1.6\,[Cr] + 1.25\,[Ni] + 1.7\,[Mn] + 1.7\,[Co] - 1.0\,[Al] \qquad (2.3)$$

Apart from the above-mentioned two stable phases there are some ordered (B2, α_2), martensitic (α′, α″) or intermetallic (γ) stable phases which are also observed in titanium alloys. These phases are regarded as not very important for the purpose of this thesis. Details of these phases can be found elsewhere [7-9].
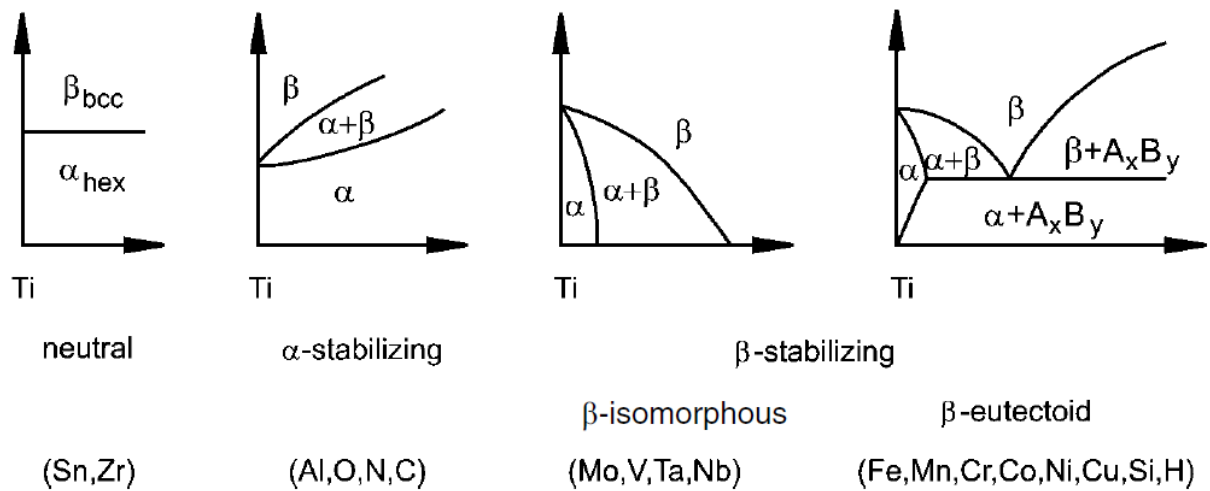
Fig. 2.3. Effect of alloying elements on phase diagrams of titanium alloys [1]

2.1.2. Metastable phases

One of the most investigated metastable phases in titanium alloys is undoubtedly the ω-phase. ω-phase in titanium alloys forms finely dispersed, submicron precipitates which are coherent with the parent β-phase. The four main conditions under which the ω-phase forms are:

1) When the β-stabilizer content is high enough to suppress the martensite start temperature below room temperature, ω-phase develops with rapid quenching. This phase is often called the athermal ω-phase.

2) ω-phase can be formed during isothermal aging in the temperature range between about 373-773 K (the range of the exact temperature can be varied by alloying elements). This phase is commonly called isothermal ω-phase. It is assumed that the isothermal ω-phase is mostly transformed from the athermal ω-phase (instead of the idea that ω athermal and isothermal phase being two completely different) [10]. The isothermal ω-phase can be distinguished from the athermal one by its slightly larger size and mainly by composition differences across β/ω interface. Aging treatment at higher temperatures results in the formation of equilibrium α-phase particles at the sites of the ω-phase particles. Phase transformations are described in section 2.3. in more details.

3) The pressure can also promote the formation of ω-phase and extends the range in which the ω-phase occurs. This pressure has to be higher than 3×10^9 Pa at room temperature for transforming the α-phase into ω-phase for very pure titanium [11].

4) Formation or increasing amount of ω-phase was also shown during deformation at room temperature in some titanium alloys (e.g. studies on Ti-Cr alloys by Bagaryatskiy [12] or on Ti-V by Brotzen [13]).

Regarding the structure of the ω-phase it either has a hexagonal structure with the space group *P6/mmm* [14] or trigonal belonging to the space group *P3m1* [15]. The hexagonal symmetry is found in leaner alloys (i.e. alloys with lower content of *β-stabilizing elements)*, while the trigonal symmetry occurs in highly stabilized alloys [2] or as an incomplete form of the hexagonal ω-phase [16]. Lattice parameters of both modifications: *a = 4.60·10^{-10} m* and *c = 2.82·10^{-10} m* with c/a ratio of *0.613*.
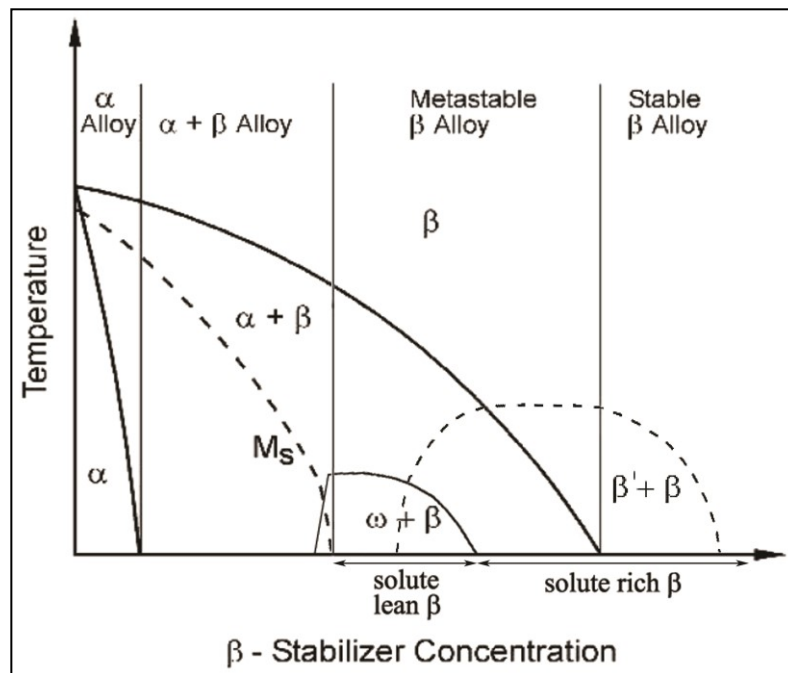

Figure 2.4.: Pseudo-binary section through a β isomorphous phase diagram showing important equilibrium and metastable phases as well as the classification of Ti alloys [2]

When the solute content of the β-stabilizing elements is sufficiently high, the metastable ω-phase becomes unstable and does not form. Instead, the β-phase undergoes a phase separation forming a *β$_{rich}$* and *β$_{lean}$*. This reaction occurs either by classical nucleation and growth or by spinodal decomposition depending on the kinetics of the reaction [8]. Both these modifications of β-phase have identical crystallographic structure as the parent β-phase; the differences occur in solute

content and lattice parameters. This reaction is schematically shown in Figure 2.4. (in literature such as on this figure β_{rich} is often denoted simply as β and β_{lean} as β').

2.2. Classification of titanium alloys

Titanium alloys can be divided into three groups - α alloys, α + β alloys and β alloys - according to the phases present at room temperature [2]. This division is also shown in the Figure 2.4.

The first group, α-alloys, contains only α-phase at room temperature. α-stabilizing elements and neutral elements are the major alloying elements in these alloys.

The so-called α + β alloys contain both α- and β-phases at room temperature. The β→α transformation is martensitic and therefore the creation of α-phase is unavoidable even after quenching to room temperature. The volume fraction of the β-phase is typically between 5 and 40 % [1]. This important group of alloys includes among others the most common Ti-6Al-4V alloy or a biocompatible Ti-6Al-7Nb alloy.

As it can be seen in the Fig. 2.4, with increasing volume fraction of β-stabilizing elements α-phase does not form during quenching to the room temperature because the M_s (martensitic start) temperature falls below the room temperature. In other words, martensitic decomposition to α-phase does not take place during quenching and therefore β-phase can be retained after quenching [2]. The β-phase in these alloys is metastable at room temperature and alloys are called metastable β -Ti alloys. In the Fig. 2.4. can be also seen that ω-phase or phase decomposition can occur during quenching to room temperature.

With high enough concentration of β-stabilizers, the β-phase becomes stable also at room temperature. It might be decomposed to β_{reach} and β_{lean} by martensitic transformation during quenching to room temperature. The practical use of these alloys is limited due to low strength without a possibility of precipitation hardening.

2.3. Phase transformations in titanium alloys

Two major mechanisms of phase transformations are known: diffusional and displacive transformations. The diffusional transformation is a reconstructive transformation in which movements of the atoms from the parent to the product lattice sites are random and occur by diffusion. This causes that the nearest atomic

bonds are broken, the new atom occupies the most appropriate position and forms a new bonds which cause the growth of the product lattice. The second type of transformation is displacive in which movements of atoms occur by homogeneous distortion, shuffling of lattice planes, static displacement waves or a combination of previous three movements. All this movements contributes to the collective motion of atoms.

Phase transformations in titanium alloys occur during thermo-mechanical processes. In this work we are dealing with metastable β-titanium alloys, therefore the most important transformations are the β→α, β→ω and ω→α transformations.

2.3.1. β → ω transformation

When a metastable β-Ti alloy, which is prone to ω-phase formation, is quenched from a temperature above the β-transus temperature to the room temperature, the so-called ω_{ath}-phase (athermal) is formed by a displacive transformation. This transformation is therefore non-diffusional and reversible [17]. During annealing at temperatures of 473–723 K particles of the ω_{iso}-phase (isothermal) are created. This is a diffusional transformation and diffusion of the β-stabilizing elements from the ω-phase particles into the surrounding β-matrix occurs during forming of ω_{iso}-phase particles.

It is well-known that ω-phase grows in certain orientation with respect to the β-phase:

$$(0001)_{\omega} \parallel (111)_{\beta} \tag{2.4}$$

$$[11\bar{2}0]_{\omega} \parallel [011]_{\beta} \tag{2.5}$$

Since four sets of $(111)_{\beta}$ planes exist, there may be four variants of the ω-phase in a given parent BCC β-phase. A model explaining the formation of the ω-phase was described by de Fontaine [17, 18].

2.3.2. β→α transformation

The β→α transformation can be diffusional or martensitic and it is controlled by two processes: migration of the α/β interface and diffusion of solute atoms across the interface.

The martensitic β→α transformation follows the Burgers orientation relations between these two phases [19]:

$$(110)_\beta \parallel (00.2)_\alpha \text{ and } [\bar{1}1\bar{1}]_\beta \parallel [2\bar{1}.0]_\alpha \tag{2.6}$$

In case of diffusional transformation, four heterogenous nucleation sites for α-phase precipitation are known in β alloys: β/β grain boundaries, previously formed α-phase particles (or α-phase martensite plates), ω-phase particles and, finally, dislocations. These nucleation sites result in a different morphology and distribution of the α-phase particles. According to various authors, three types of nucleation mechanisms are distinguished based on the ageing temperature and nucleation site [20, 21].

1) At relatively low aging temperature (< 723 K), very fine α-phase particles precipitate in the matrix because the precipitation is energetically appropriate. Due to the size and distribution it is assumed that ω-phase is a precursor of the creation of the α-phase. This ω→α transformation is described in the section 2.3.3. in detail.

2) At temperatures above 823 K, the ω-phase particles are already dissolved. The thermal activation is sufficient for the homogeneous precipitation of the α-phase particles within β grains, which grow to the shape of lamellae. α-phase may also precipitate heterogeneously along grain boundaries.

3) At high aging temperatures (> 923 K) the α-phase particles do not precipitate homogeneously within the grains. The diffusivity for precipitation is sufficient; on the other hand, the driving power of precipitation is not enough at above-mentioned temperatures (just below β-transus temperature). α-phase precipitates only heterogeneously along the β/ β grain boundaries and lamellae then grow to the grains interior perpendicularly to these inter granular α-phase particles [22].

2.3.3. ω→α transformation

Three nucleation sites of the formation of α-phase precipitates from the ω-phase particles are well-known from the literature:

1) At the ω/β interfaces. This α-phase nucleation is typical for high misfit systems which exhibit cuboidal shaped ω-phase particles [9] and it was precisely studied by Williams and Blackburn [23].

2)   Directly from the ω-phase particles by a monotropic reaction [9]. This regime was observed during ageing at temperatures where the ω-phase is stable for relatively short times.

3)   Due to α-stabilizing element, Al enrichment in the region near to ω/β interface. This enrichment could arise from the interaction of the stress field associated with the ω/β interface and the diffusion of solute elements [24].

3.   Ultra-fine grained materials

3.1. Fundamentals and properties

Ultra-fine grained materials are defined as polycrystalline materials with grain sizes lower than 1 μm but typically greater than 100 nm. Moreover, ultra-fine grained materials are characterized by homogeneous microstructure and a high proportion of high-angle grain boundaries. These materials usually have excellent mechanical properties - strength, hardness, fatigue resistance. The often disadvantage is the reduced ductility of the material [25].

The reduction of grain size in polycrystalline materials cause changes in mechanical and physical properties. At ambient temperatures, the strength generally follows the Hall– Petch relation [26, 27] so that

$$\sigma_y = \sigma_0 + k_y d^{-1/2}, \qquad\qquad (3.1)$$

where σ_y is the yield stress of the material, σ_0 represents the friction stress, k_y is a material constant and d is a size of grains.

Metals with grain size lower than 1 μm can be basically produced by two ways [28]. The first method is so-called "bottom-up" approach where the polycrystalline metal components are made up from individual atoms by deposition techniques or produced by nanoscale building blocks, for example, the gas atomization followed by sintering. Disadvantages of these techniques are very small samples usually containing some residual porosity. The second procedure is the "top-down" approach in which bulks of fully-dense coarse-grained solids are processed by severe plastic deformation (SPD) methods introducing a high dislocation density to the material without any concomitant change in cross-sectional dimension of the sample. According to this approach, dislocations are capable to re-arrange into dislocation walls and subgrain boundaries, which may eventually evolve into high-angle grain boundaries by progressive lattice rotation. Typical achievable sizes of grains lie in ultra-fine grained range (100 nm - 1 μm) or even in true nanometer range (<100 nm) [29].

The most important SPD method, equal channel angular pressing (ECAP) was developed and successfully applied by V. M. Segal [30]. Currently, in addition to the ECAP, also used SPD methods are the following: high pressure torsion (HPT) [31], accumulative roll bonding (ARB) [32] and many others. For this thesis, the most

important technique is the high pressure torsion (HPT). This method has been used for more than twenty years for the preparation of ultra-fine grained aluminium, magnesium or steels. Ultra-fine grained pure titanium and the most used titanium alloy Ti-6Al-4V were later also prepared by these methods [33 - 36].

3.2. High pressure torsion (HPT)

During high pressure torsion (HPT) a disc-shaped sample with a diameter of typically 10 mm or 20 mm and a thickness of approximately 1 mm is placed between two anvils which compress the sample at high pressure (several GPa). Afterwards, one of the anvils is rotated (approximately 1 revolution per minute) which consequently leads to torsion of the sample. The schematic representation of the procedure is shown in the Fig. 3.1. The total strain imposed by HPT in the sample can be expressed in two ways. The first one (Hencky/Eichinger) is can be expressed by the logarithmic relation [37]:

$$\varepsilon_{Hencky} = \ln\left(\frac{2\pi Nrh_0}{h^2}\right), \tag{3.2}$$

where N is the number of rotations, r represents the radius of the sample, h_0 and h its initial and final thickness, respectively.

The second von Mises-approach is using a simple torsion and can be expressed by the linear relation [38]:

$$\varepsilon_{von\ Mises} = \frac{\gamma}{\sqrt{3}} = \frac{r\theta}{\sqrt{3}h} = \frac{2\pi Nr}{\sqrt{3}h}, \tag{3.3}$$

where γ is the shear strain and θ is the rotation angle.

Due to the geometry of the deformation the induced deformation increases from the centre to the edge of the sample. It is also possible to produce samples by different numbers of revolutions HPT (typically e.g. N = ¼ turn, ½, 1, 3, 5, 10) – so with different induced deformation. HPT is usually carried out at the room temperature, but may be also performed at elevated temperatures according to the configuration of the device. The main advantage is the high degree of embedded deformation. Disadvantages are the small size of samples and inhomogeneous deformation which prevents the industrial production [39]. The application of material produced by HPT is very limited due to small sizes of the samples, though manufacturing of micro-devices is possible as mentioned in [29].
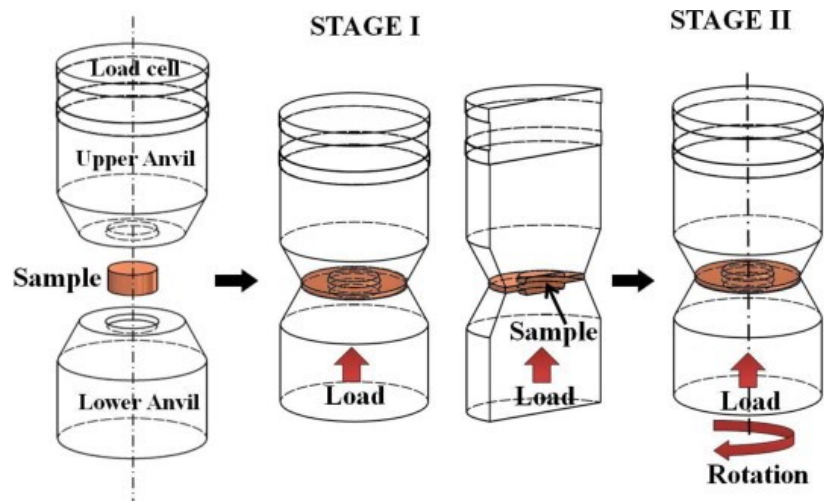
Fig. 3.1. Schematic representation of HPT [40]

3.3. Ultra-fine grained titanium and titanium alloys

Ultra-fine grained titanium was first prepared by the method of intensive plastic deformation at Ufa State Aviation Technical University (USATU), Ufa, Russia nearly two decades ago [41]. Increased strength of ultra-fine grain titanium has recently been used as an advantage in manufacturing of dental implants [42].

However, only in the last three years ultra-fine grained metastable β-Ti alloys were prepared. Experimental work has so far focused primarily on the study of the mechanical properties of ultra-fine grained material [43, 44]. Microstructural stability was investigated only rarely and only for alloys that contain niobium as the main alloying element, which suppresses the formation of ω-phase [45,46].

Author of this thesis has already dealt with mechanical properties of ultra-fine grained α+β titanium alloy, Ti-6Al-7Nb in her bachelor thesis [47].

4. Experimental materials

4.1. Metastable β-Ti alloys

Recently, metastable β-Ti alloys have been attracting an increasing attention. The main use of β-Ti alloys currently belongs to the aircraft industry, in which these alloys are gradually replacing more common Ti-6Al-4V alloy.

The use of β-Ti alloys in orthopaedics is also expected, since – compared to Ti-6Al-4V alloy – they have a lower Young´s modulus which better corresponds with the Young´s modulus of bones (10-30 GPa) [1].

The mechanism of grain refinement in β-titanium alloys can vary widely, depending on the specific alloy composition and β-grain size [48]. The classical mechanism of grain refinement is based on the movement of dislocations, formation of dislocation walls and sub-grain boundaries, which evolve to grain boundaries possibly by subgrain rotation mechanism. This process occurs during deformation and is continuous in its nature, but may not require significant thermal activation and therefore does not fulfil common definition of dynamic recrystallization [49]. Grain refinement can also be induced by twinning. Primary twins can be formed in the matrix, subsequently secondary twins are formed within the primary twins and so on. Ultra-fine grain structure can be formed by consequent lattice rotation. For example, in commercially pure Ti the twinning-induced grain refinement was proven by Zherebtsov et al. [50-52]. The twinning-induced grain refinement mechanism was not proven in β-Ti alloys yet.

4.2. Ti-15Mo alloy

One of the studied alloys was a binary Ti-15Mo alloy with 15 wt. % of molybdenum. Chemical composition of Ti-15Mo alloy is summarized in Table 4.1.

The *Mo* is β-stabilizing element and in the Ti-15Mo alloy the molybdenum content is high enough to suppress the martensitic β to α transformation below room temperature which makes the Ti-15Mo alloy metastable β-Ti alloy.

Element	Composition (wt. %)
H_2	0.001
N_2	0.014
0_2	0.185
Fe	0.030
C	0.007
Mo	15.200
Ti	Balance
Si	0.090

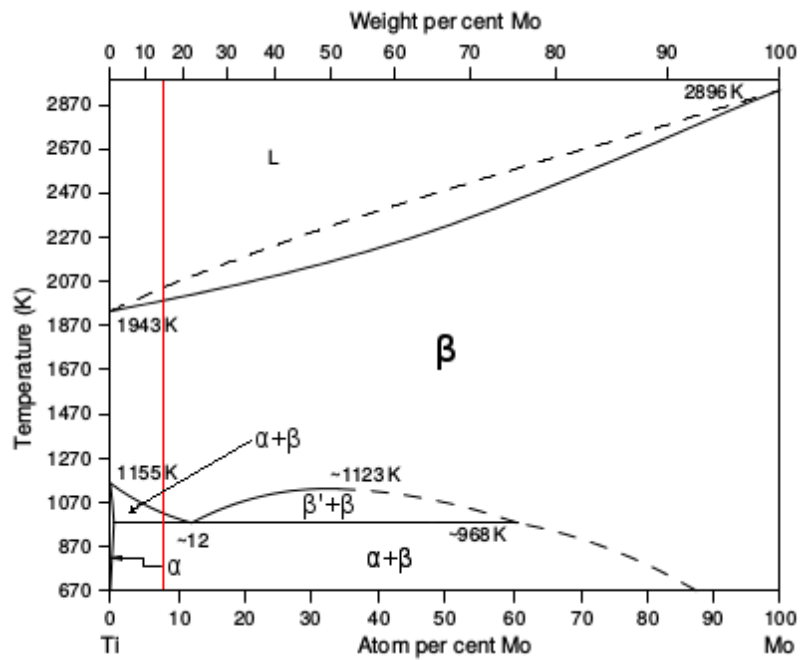Table 4.1. Chemical composition of Ti-15Mo alloy [53]

Fig. 4.1. Equilibrium phase diagram of Ti-Mo system [7]

In the Fig. 4.1. the equilibrium phase diagram of Ti-Mo system is shown . The red line represents the chemical composition of the studied alloy. The phase transformation from α+β to β-phase occurs approximately at 1023 K.

Some specific properties are summarized in the Table 4.2. [54, 55].

Density (mg/cm³)	4.96
β-transus temperature (K)	1063
Modulus of Elasticity in Tension (GPa)	78 (β) 105(α+β)
Elongation (%)	20
UTS [MPa]	690

Table 4.2. Typical properties of Ti-15 Mo alloy [54]

The alloy procured from Carpenter Co. was solution treated at 1083 K/4h [56]. Samples were subjected to HPT method using pressure of 4 GPa at room temperature. Samples of 20 mm in diameter were processed by ¼, ½, 1, 3, 5 and 10 turns of HPT.

4.3. TIMETAL LCB alloy

The second alloy which was investigated is TIMETAL LCB. This alloy was developed by TIMET Ltd. and is classified as a metastable β-Ti alloy. The name (low cost beta) suggests the price reduction which was achieved by using Fe or Mo as β-stabilizing element instead of expensive elements such as V or Nb.

The chemical composition of the material is shown in Table 4.3.

Element	Composition (wt. %)
Ti	87.20
Mo	6.80
Fe	4.50
Al	1.50
N	0.01
O	0.16

Table 4.3. Chemical composition of TIMETAL LCB [57]

Typical properties, comparing with Ti-15Mo alloy are listed in Table 4.4. [58, 59].

Density (mg/cm^3)	4.8
β-transus temperature (K)	1063
Modulus of Elasticity in Tension (GPa)	110-117
Elongation (%)	16
UTS (MPa)	1035

Table 4.4. Typical properties of TIMETAL LCB alloy

The alloy was treated analogously that in case of Ti-15Mo alloy, e.g. at 1083 K/4h [56]. Samples were subjected to high pressure torsion of 4 GPa at room temperature. Samples of 20 mm in diameter were processed by ¼, ½, 1 and 5 turns of HPT.

5. Experimental methods

5.1. Sample preparation

For the purpose of this study, two titanium alloys Ti-15Mo and TIMETAL LCB were used. The rods with diameter of 19.5 mm were first sealed in quartz tube filled with argon, solution treated (1083 K, 4h) and consequently water quenched. Rods were cut to discs with thickness of 1 mm and deformation by HPT was carried out at Ufa State Aviation Technical University (USATU) Ufa, Russia at room temperature and pressure (see Chapter 4). In case of Ti-15Mo alloy samples after ¼, ½, 1, 3, 5, 10 turns and in case of TIMETAL LCB alloy specimens after ¼, ½, 1, 5 turns of HPT were prepared.

The samples after HPT are discs of approximate thickness of 0.8 mm and diameter 20 mm. However, the material during HPT was leaking off. This leaked part of the sample was removed by cutting-off using Struers Accutom-50 and grinding on 80 grit (European FEPA grading) SiC grinding paper to get 20 mm diameter samples.

The method of sample preparation differs for each experimental method. Therefore, the methods of preparation are specified in the description of each method.

5.2. Microhardness measurement

Microhardness measurement was carried out on microhardness tester Qness Q10a by Vickers method. In the Vickers method, the diamond indenter with the form of a square-based pyramid and with the top angle between sides equal to 136° is used. The schematic illustration of Vickers method is shown on Fig. 5.1.
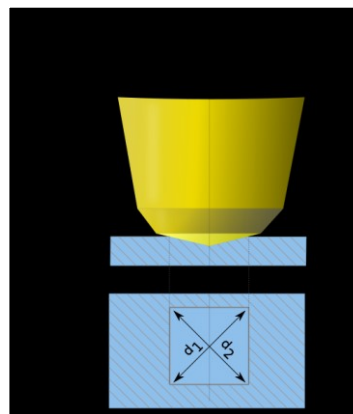

Fig. 5.1 Vickers microhardness scheme [60]

Firstly, the indenter is pressed into the surface of the specimen with a specified force. A surface area A of an indentation imprint can be expressed by the formula

$$A = \frac{d^2}{2\sin\left(\frac{136°}{2}\right)},\tag{5.1}$$

where d means the average length of the diagonal of the indentation imprint in millimetres. The equation (5.1) can be approximated to give

$$A \approx \frac{d^2}{1.8544}\tag{5.2}$$

The resulting microhardness value (HV number) is determined by the ratio F/A

$$HV = \frac{F}{A} \approx \frac{1.854F}{d^2},\tag{5.3}$$

where F is the applied force in kilogram-force (kgf). The physical unit of such HV number is kgf/mm^2. Measured value must be multiplied by 9.81 (standard gravity) to get HV in MPa. Moreover, very simple rule of thumb for many metallic materials reads that HV value in MPa divided by a factor of 3 corresponds approximately to the ultimate strength of the material in tensile test.

We used a 1 kg load and indentation time of 10 s. In the Fig. 5.2., the typical indent is shown. The indents were evaluated automatically with 400x magnification, automatic focusing and automatic brightness adjustments.
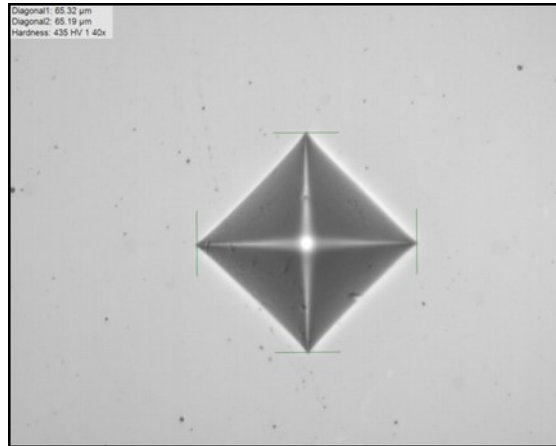

Fig. 5.2. Typical indent with 400x magnification after automatic evaluation
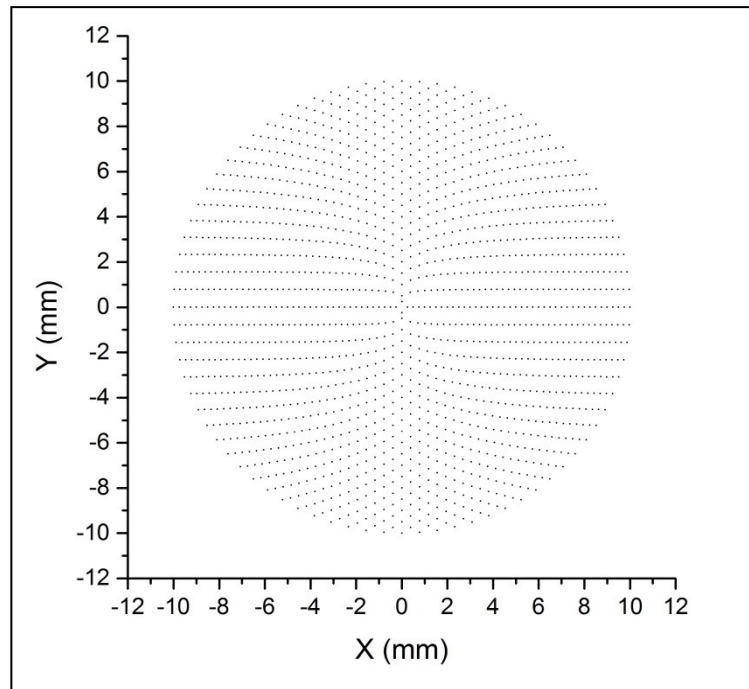
Fig. 5.3. Schematic illustration of distribution of indents

More than 1000 indents were applied on disc-shaped specimen with the diameter of 20 mm. The scheme of distribution of indents is illustrated in Fig. 5.3. Despite it is not apparent from the figure, the scheme consists of concentric circles with mutual distance of 250 microns. Circles are then divided into points such that the minimum distance between the points along the circle perimeter is bigger than 350 microns. This special pattern for microhardness mapping of HPT samples was developed in AutoCAD software. This distribution allows investigating the radial dependence of microhardness from the centre of the sample.

Due to an inhomogeneous deformation during HPT, the microhardness is also inhomogeneous. The increasing microhardness with increasing distance from the centre of the specimen (i.e. with increasing strain) is expected. The deformation of each specimen can be represented by colour-coded polar diagrams which were prepared for each sample by program OriginPro. The change of the microhardness with increasing distance from the specimen centre and the number of HPT turns can be also depicted using so-called radial diagram. For each sample, the HV values of points on one concentric circle were averaged, i.e. one value from each 250 microns increment of distance from the centre were obtained. The microhardness after various number of HPT rotations can be compared on radial diagrams.

20

Microhardness was also evaluated for the cross-section of the sample. Samples for this measurement were cut-off from the disc-shaped sample as shown in Fig. 5.4.
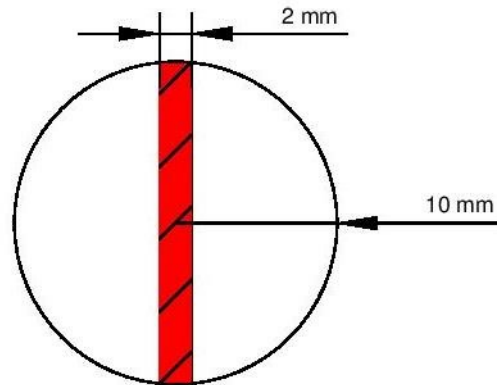

Fig. 5.4. The scheme of cutting-off of the cross-section of the sample for the microhardness measurement, prepared in AutoCAD software. Cut stripe was polished from the side (i.e. cross-section of the HPT processed sample).

More than 800 indents were applied on the cross-section specimen in a square grid. The microhardness evaluation was again done by program OriginPro. The change of the microhardness with increasing distance from the surface of the sample is shown on XY contour diagram.

Microhardness measurement was performed on the sample just before the SEM observations. The preparation of samples therefore follows the preparation for SEM observation and is described in details in Chapter 5.2.

5.3. Scanning electron microscopy (SEM)

Direct observations of the microstructure of HPT processed samples were accomplished by scanning electron microscope FEI Quanta 200F at 10 kV.

The source of electrons in the microscope is a field emission gun (FEG). The electrons which were emitted from the cathode (FEG) are accelerated by voltage of 10 kV. This primary electron beam hits the sample and the electrons interact with the atoms of the material. This interaction is reflected in the formation of different signals which can be detected. These signals give information about the topology or composition of the sample.
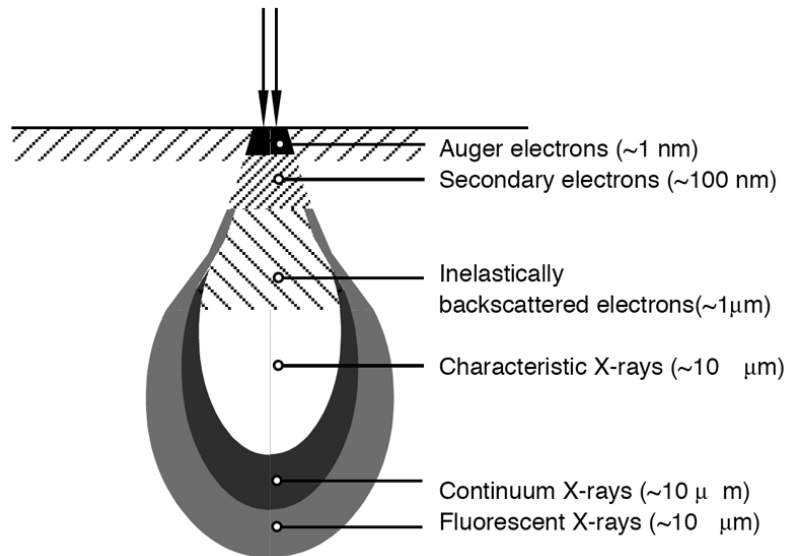
Fig. 5.5. Bulk penetration of primary electrons [61]

The first type of signal which can be detected are back-scattered electrons (BSE) with energy >50 eV. BSE are utilized to investigate the chemical contrast of the sample. This contrast is given by chemical composition – so-called Z-contrast. The Z-contrast is caused by the different atomic number of elements. Heavy elements (with bigger atoms) scatter electrons more likely than lighter elements and therefore more electrons are back-scattered closer to the surface. As a result back-scattered electrons from heavier elements get back from the sample to the detector more likely. Lighter elements scatter electrons in average deeper in the specimen. Not all of these back-scattered electrons can exit the sample due to further scattering in the specimen and therefore the number of back-scattered electrons is lower. For that reason, lighter elements appear darker in the BSE image.

An alternative technique for characterizing materials in SEM is electron channelling contrast imaging (ECCI). ECCI is produced from electrons which channel down the crystal planes [62]. Channelling assumes that crystal lattice can be described in terms of channels or paths where the electron can preferably penetrate to a higher depth before scattering. Thus certain orientations of the crystal will back-scatter more electrons than others, giving rise to orientation contrast. If the electron beam is lined up with the crystal channels, electrons penetrate more deeply and the number of back-scattered electron is reduced. These channels are closed already for the slightly tilted crystals; similarly distortion of crystal planes may close these channels.

Another type of signal which can be detected are low-energy (< 50eV) secondary electrons (SE). After inelastic scattering of the primary electron with an atom in the sample, secondary electrons are emitted from the electron shell. Due to the low energy of these electrons they originate within a few nanometers from the surface of the sample (see Fig. 5.5.). The amount of emitted secondary electrons reflects the topology of the surface of the sample. If the beam enters the sample perpendicular to the surface, then the activated region is uniform around the axis of the beam, electrons can penetrate deeper to the sample and the probability of the exit of the secondary electron to the surface is lower. As the angle of incidence increases, the "exit distance" of one side of the beam will decrease, and more secondary electrons will be emitted. Thus steep surfaces and edges tend to be brighter than flat surfaces, which results in images with a well-defined, three-dimensional appearance.

Primary electron also interacts with the inner electronic shell of atoms ejecting the electron from its orbital. Then the inner shell vacancy can be filled by an electron from an outer, higher energy shell. The energy difference between the two shells can be released in two ways. In the Auger process, the energy is used to eject another outer shell electron. In the characteristic X-ray process, the excess energy is released in the form of a characteristic X-ray radiation [63]. Energy dispersive X-ray spectroscopy (EDX) is used for the chemical characterization of the sample by detecting emitted X-ray radiation. Characterization of individual elements is based on the fact that each element in atomic structure has a unique set of peaks in its X-ray spectrum [64].

5.3.1. Electron back-scattered diffraction (EBSD)

Electron back-scattered diffraction (EBSD) is a method which provides information about the microstructure of material and orientation of grains. For example, texture, grain size, misorientation of grains and many other features may be acquired from EBSD results.

For an EBSD measurement, focused beam is used to get information about each point of the sample. The specimen is placed in the SEM chamber at a highly tilted stage (~70° from horizontal) towards the EBSD camera, to increase the contrast in the resultant electron back-scatter diffraction pattern. In this configuration, some of the electrons inelastically scatter in the sample and get back to the surface and to the CCD camera. As these scattered electrons escape from the sample, they may exit

at the Bragg condition [49] related to the spacing of the periodic atomic lattice planes of the crystalline structure and diffract. An electron back-scatter diffraction pattern (EBSP) is formed when many different planes diffract different electrons to form Kikuchi lines which correspond to each of the lattice diffracting systems of planes. Each Kikuchi band can be indexed by Miller indices [49]. According to the shape of Kikuchi lines, the crystallographic orientation of the material in given point can be evaluated using so-called Hough transformation and dedicated software procedure. Crystallographic orientation might be associated with specific colour according to the orientation triangle and so-called inverse pole figure map can be created.

The scanning electron microscope (SEM) FEI Quanta 200 FX equipped with EDAX camera and OIM software was utilized for EBSD observations. The employed acceleration voltage was 10 kV.

Sample preparation included grinding by 500, 800, 1200, 2400 grit SiC papers by Struers. Afterwards, the samples were polished on Vibromet vibratory polisher (Buehler) using polishing suspension Alumina of grade 0.3 μm and 0.05 μm. Finally, to achieve clean and absolutely flat sample a Colloidal Silica was used. Samples were polished on vibratory polishing for each step around 8 hours.

5.4. Positron annihilation spectroscopy (PAS)

Positron annihilation spectroscopy (PAS) is a non-destructive method to study defects in material. The PAS technique is based on the principle that positron annihilates through interaction with electron in material.

The radioactive source decays by β^+-decay during which the positron is created. At the same time, the radioactive source also emits a γ-photon – it is a so-called start signal. The positron enters to the material and thermalizes in the sample. This thermalization means that energy of the photon decreases from ~ 100 keV to ~ 0.03 eV and it takes only ~10 ps time. Afterwards, if the positron encounters the electron, it annihilates by emitting two γ-photons. One or both these photons are detected as a stop signal by one or two detectors. The time between stop and start signal is defined as the positron lifetime. The measurement of the positron lifetime is schematically shown in the Fig. 5.6.
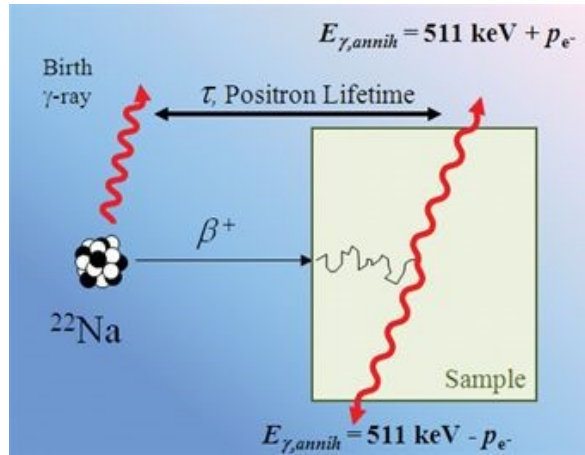
Fig. 5.6. Schematic representation of measurement of positron lifetime [65]

In a defect free lattice, the electron density is higher and the positron lifetime is shorter. If material contains defects, such as vacancies, the positron can be trapped in the defect. The electron density around defects is lower, the probability of annihilation of electron and positron is also lower and the average positron lifetime is longer. As a consequence, mean positron lifetime correlates with the density of individual lattice defects. The example of measured statistics of the positron lifetime can be seen in the Fig 5.7. The positron lifetime spectrum can be divided into components associated with different lifetimes. These mean lifetimes are ascribed to different types of defects, whereas the intensities of the components give us information about concentrations/densities of different defects. The decomposition of lifetime spectrum is done by fitting the two-state simple trapping model (STM) [66]. This model assumes that only trapping of the thermalized positrons occurs, release of the trapped positrons does not occur, defects are distributed homogenously in the sample and the trapping in defects is limited by cross-section of the quantum transition.

The fitting function S is defined as:

$$S(t) = \left(\sum_{i=1}^{n} \frac{I_i}{\tau_i} e^{\frac{-t}{\tau_i}} \right) \otimes R(t) + B \tag{5.4}$$

The function describes a sum of contributions from free positrons (positrons annihilated in a defect-free lattice) and positrons trapped in various types of defects. I_i is the count of the detected photons (intensity) attributed to each contribution, and τ_i is the appropriate mean lifetime of either free positrons or positrons in different types of defects. R is the resolution function of the detector and B is the background,

25

i.e. the random coincidences. The quantities *R* and *B* are given, whereas all intensities and lifetimes are fitted.
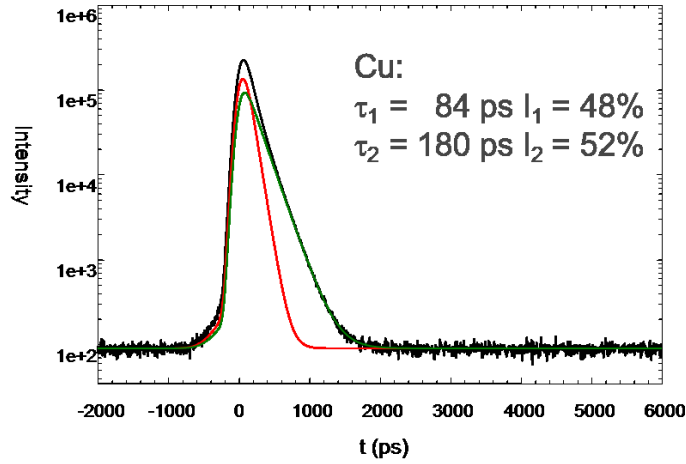

Fig. 5.7. Positron lifetime spectrum. Note the logarithmic scale of the vertical axis. Black curve are the measured data. Red curve shows the fitted contribution of free positrons, whereas the green curve is the contribution of positrons annihilated in dislocations [67]

For example, in the Fig. 5.7., the measured and fitted positron lifetime spectra for pure Cu are shown. The mean lifetime of free positrons τ_1 is lower than τ_2 which belongs to lifetime of positrons trapped in dislocations. Fitted lifetime of dislocations can be then compared to theoretical value computed from theoretical model [68].

Equation (5.5) is used for verifying the assumptions of the two-state trapping model [69]:

$$\frac{1}{\tau_B} = \frac{I_f}{\tau_f} + \sum_{i=1}^{N} \frac{I_i}{\tau_i}, \tag{5.5}$$

where τ_B is the mean positron lifetime measured for a defect-free material. Note than in the defect-free material all positrons annihilate as free-positrons, which is characterized by single lifetime τ_B. With increasing concentration of defects, the mean lifetime of positrons annihilated as free-positrons is reduced. τ_f and I_f correspond to the measured positron lifetime of free positrons in investigated material and intensity of this contribution, respectively. τ_i and I_i correspond to lifetimes and intensities of positrons trapped in various defects, respectively. Note that with increasing concentration of defects, measured lifetime of free positrons τ_f decreases. If the measured variables fulfil equation (5.5), then the two-state simple trapping model can be used for analysis of defect structure of material.

Another type of measurement by annihilation of positrons is measuring of the Doppler broadening (DB), which is a difference in energies of γ-photons emitted after annihilation of positron-electron pair caused by non-zero momentum of interacting particles. Since the energy of thermalized positron is negligible, the energy broadening is given by the momentum of the electron, more specifically, by the longitudinal part of the momentum, which is the part of momentum parallel to the direction of emitted γ-photons. The difference in energy can be expressed by formula (5.6):

$$\Delta E = \frac{1}{2} p_L c,$$ (5.6)

where p_L is the longitudinal part of momentum of electron and c is the speed of light. The tabulated energy of γ-photons is 511 keV. In real, the deviation from the tabular value is ~1 keV. If the positron annihilates with low-momentum valence electrons, the Doppler broadening is lower, for the high-momentum core electrons it is quite opposite. To quantify this effect, so-called S parameter is introduced. The S parameter is calculated as the ratio between area near the centre of the peak and the total area of the peak (the centre part of the area in the Fig. 5.8. is highlighted with grey colour, the red line defines the background). The S parameter therefore expresses the proportion of the annihilation of positrons with low-momentum valence electrons. Increased S parameter therefore generally means increased amount of defects.
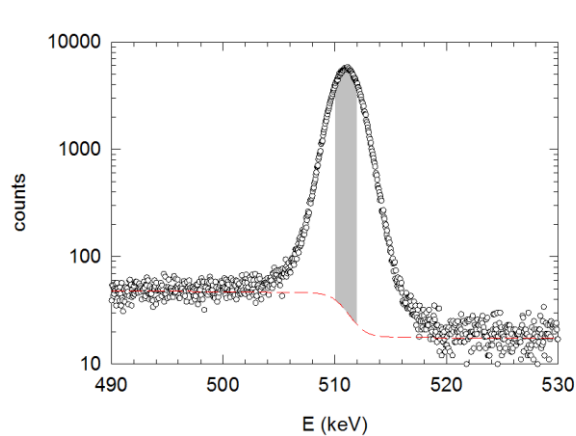

Fig. 5.8. DB spectrum with highlighted part of the annihilation with valence electrons [70]

In the opposite case, if positron annihilates with high-momentum core electrons the Doppler broadening is higher. For the expression of the proportion of

the annihilation of positrons with core electrons the W parameter is used. The W parameter is calculated analogously as the S parameter. (The portion of the W parameter is schematically illustrated in the Fig. 5.9). Decreasing W parameter means increasing amount of defects.
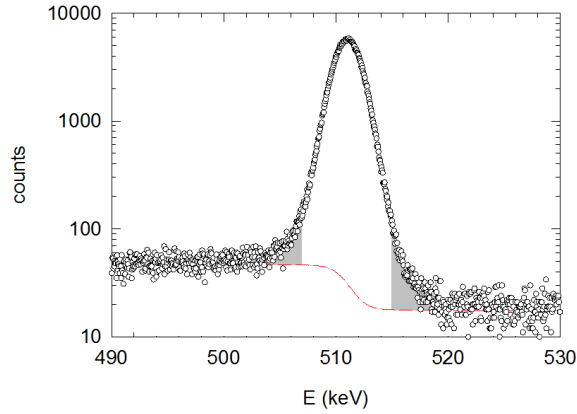

Fig. 5.9. DB spectrum with highlighted part of the annihilation with core electrons [70]

A correlation plot of S and W parameter (the so-called S–W plot) is useful for detecting the change in the nature of positron trapping defects and it allows identifying the annihilation site.

The simple trapping model can be also used for determining the dislocation density in material. For simplicity we assume that the material contains only one type of effect (dislocations) and defect-free matrix. The positron trapping rate K_D to dislocations is defined as:

$$K_D = I_D \left(\frac{1}{\tau_f} - \frac{1}{\tau_D} \right),$$

(5.7)

where τ_f is the lifetime component of free positrons and τ_D is the component of the lifetime attributed to the positrons trapped at dislocations. I_D is the intensity of the positrons trapped at dislocations. Note that the trapping rate can be computed only in presence of free-positron lifetime component. Once this component disappears (i.e. dislocation density is high such that virtually all positrons are trapped in defects before annihilation), the trapping rate cannot be calculated, which causes a certain upper limit for dislocation density determination. The trapping rate is directly proportional to the dislocation density ρ_D defined by (5.8):

$$\rho_D = \frac{1}{\nu_D} K_D,$$

(5.8)

where v_D is the specific trapping rate to dislocations, which is a constant and fall into the range from 10^{-5} to $10^{-4}\,\mathrm{m^2s^{-1}}$ for most metals [71].

The density of dislocations can be also calculated from the DB results. The S parameter can be defined:

$$S = (1 - F_D)S_0 + F_D S_D \tag{5.9}$$

S_0 is the S parameter for annihilation of free positrons, S_D is the S parameter for positrons trapped at dislocations and finally F_D is the fraction of positrons annihilated at dislocations and is related to the positron trapping rate according to the relation:

$$F_D = \frac{K_D}{K_D + \frac{1}{\tau_B}} \tag{5.10}$$

Combining equations (5.9), (5.10) and (5.8) the dislocation density can be calculated from DB data using the expression:

$$\rho_D = \frac{1}{v_D \tau_B} \frac{S - S_0}{S_D - S} \tag{5.11}$$

The Doppler broadening measurement of S parameter is much faster (less data are required to achieve sufficient statistics) than positron lifetime measurement. Therefore this approach of dislocation density evaluation is very useful for studied HPT samples, where many measurements for different induced deformation conditions are required even on a single sample.

The lifetime of positron and Doppler broadening on HPT samples of Ti-15Mo alloy was measured in collaboration with Department of Low Temperature Physics of the Charles University in Prague. The $^{22}Na_2Co_3$ radioactive source deposited on a 2µm thick mylar foil was used. The radioactive source $^{22}_{11}Na$ decays by β^+-decay in a following way:

$$^{22}_{11}Na \rightarrow {}^{22}_{10}Ne + e^+ + v_e, \tag{5.12}$$
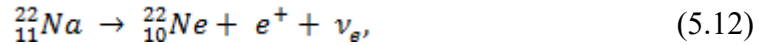
where e^+ is a positron and v_e is electron neutrino. The half-life of this source is 2.6 years. The start γ-photon has energy of 1274 keV and stop γ-photons have energy of 511 keV each.

The source is placed between two identical samples of the studied alloy. Positron lifetime was measured by fast-fast spectrometer [72] with a time resolution of 150 ps (FWHM ^{22}Na). The construction of measuring DB consists of the HPGe (semiconductor) detector which measures the energies of γ-photons. The signal is amplified and the ADC converts the pulse to digital number of the difference of energies.

5.5. Differential scanning calorimetry (DSC)

Differential scanning calorimetry (DSC) developed by Watson and M. J. O'Neill around 1962 is one of the most widely used thermoanalytical measuring method. During DSC measurement the measured and a reference sample are simultaneously and linearly heated or cooled usually in special ceramic crucibles. Measured sample and reference sample are placed in identical environments. The reference sample must have a well-defined thermal capacity during whole measurement. Therefore, pure material or even an empty crucible is often used as a reference. Calorimeter indicates the difference of heat which is needed to give to the sample towards the reference.

The DSC signal (heat flux) is plotted as a function of temperature or time and indicates the heat exchange. If first order phase transition is associated with detectable exothermic or endothermic heat effect, then it is identified by DSC. DSC curves are directly associated with the change of the enthalpy. The type of the transition (endothermic or exothermic) determines whether heat is absorbed or released. The heat absorbing events are such as melting or dissolution and heat releasing solidification or precipitation. In our case peaks directed upwards on the DSC curve correspond to the exothermic reaction, the downward peaks to the endothermic ones.

The differential scanning calorimetry measurements were performed on Netzsch calorimeter DSC 404 Pegasus. The sample was held in a dynamic argon atmosphere during the measurement. The selected heating rate was 5 K/min from room temperature up to 1023 K.

Samples for DSC measurement were prepared from Ti-15Mo alloy from non-deformed material (solution treated) and material after HPT N = 1 rotation. Specimens of dimensions 3.5x3.5x1 mm were cut-off using Struers Accutom-50. Fig. 5.10. illustrates the method of the cutting-off samples from disc-shaped HPT samples. Non-deformed samples were cut in similar way to get samples with the same dimensions as samples after HPT. Afterwards, samples were grinded and polished up to 800 SiC grit paper to get all samples with approx. the same weight for comparing the DSC signals.
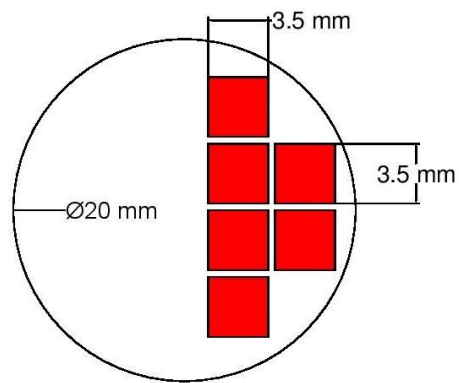
Fig. 5.10. Schematic illustration of cutting-off samples for DSC measurement
(scheme was prepared in AutoCAD software)

6. Aims of the thesis

The ultimate goal of the research in the present work is the characterization of the microstructure and physical properties of Ti-15Mo and TIMETAL LCB alloys after deformation by HPT. The motivation for this research was the extension of current knowledge about ultra-fine grained Ti alloys processed by severe plastic deformation.

The aim of the present work is to study the influence of the deformation by HPT on the microstructural characteristics, microhardness, defect evolution and phase transformations in studied alloys.

This thesis focuses in detail on:

- The microhardness evolution with HPT rotations and with distance from the centre of the sample
- Ability of deformation strengthening of both alloys
- The observation of the deformed microstructure of both alloys by scanning electron microscopy and electron back-scattered diffraction
- Description of the mechanism of twinning-induced grain refinement in ultra-fine grained Ti-15Mo alloy
- Investigation of the defect structure in the Ti-15Mo alloy
- Effect of the HPT deformation on the phase transformations in Ti-15Mo alloy

7. Results and discussion

7.1. Microhardness measurements

The microhardness evolution in all samples of Ti-15Mo and TIMETAL LCB alloys deformed by HPT was measured. A series of colour-coded images is used for presentation of microhardness evolution and the colour bar scale is the same for all measurements.

7.1.1. Ti-15Mo alloy

In the Fig. 7.1. the microhardness evolution with increasing number of HPT turns is depicted. The colour-coding reflects the microhardness variations within each sample. Two distinct regions are readily apparent – a central region with low microhardness and the peripheral region with increased microhardness. The microhardness in peripheral region increases with increasing amount of HPT turns. In the region close to the specimen edge, lower microhardness occurs (especially in specimens after $N = ¼$ and $N = 1$ HPT turns) because of the leaking off the material during HPT process. Therefore, in the material near to the edge, the induced deformation is in fact lower as well as the microhardness.

By radial averaging of HV values, line profiles of Vickers microhardness were obtained as shown in the Fig. 7.2. It is demonstrated, that the microhardness increases with increasing distance from the centre (with exception of the region close to the edge) and that in peripheral part, the microhardness increases with increasing number of HPT turns. The distribution of microhardness remains heterogeneous even after $N = 10$ HPT turns. The minimum achieved microhardness in the specimen centre ($HV \approx 330$) and maximum achieved values in the peripheral regions ($HV \approx 450$) shall be compared to the microhardness values achieved by precipitation hardening, which is the most used strengthening method in beta Ti alloys [1].
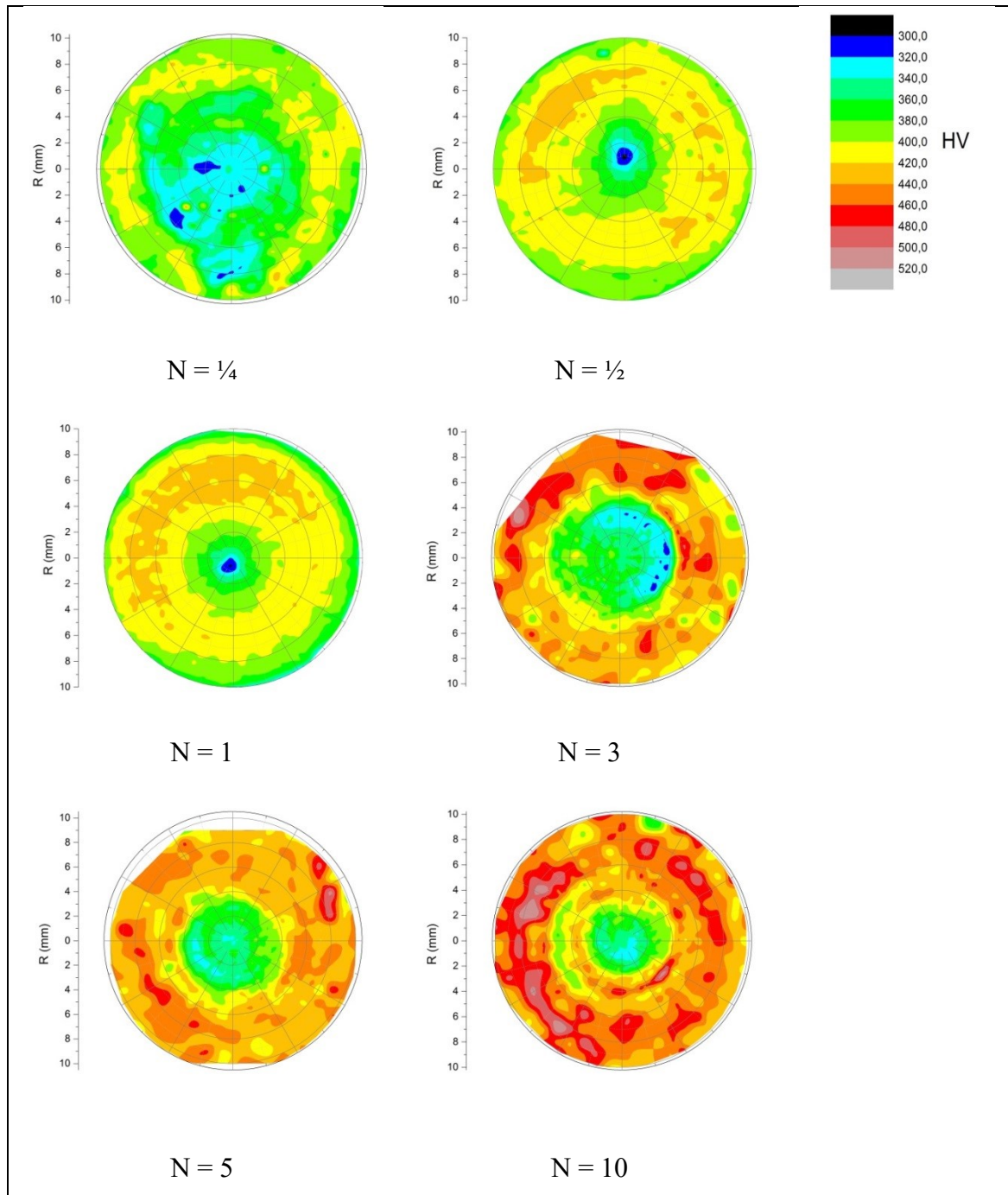
Fig. 7.1. Microhardness of Ti-15Mo alloy after various number of HPT turns represented on colour-coded polar diagram
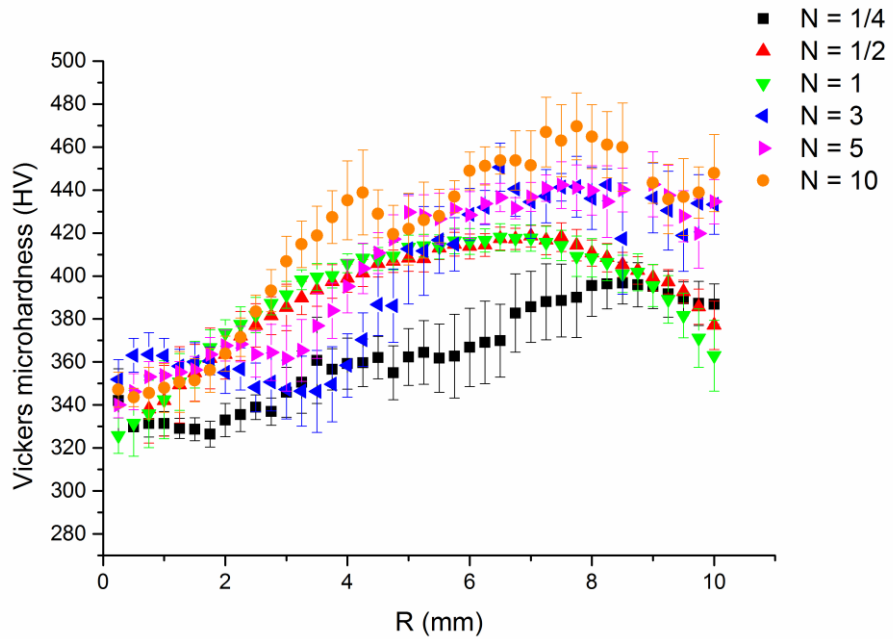
Fig. 7.2. Radial dependence of Vickers microhardness of Ti-15Mo alloy for various HPT rotations

The microhardness of cross-section of the specimen was measured on different samples than microhardness evaluated over whole discs. Thus, the distribution of the microhardness of the cross-section along the diameter of may not be in accordance with the distribution of microhardness of the disc-shaped samples.

Fig. 7.3. represents the Vickers microhardness of cross-section of Ti-15Mo alloy. The increase of microhardness in the peripheral regions with increasing number of HPT rotations is clearly visible such as the increase of microhardness with increasing distance from the centre of the specimen. On the other hand, higher microhardness in central part of N = 1 compared to N = 3 remains unclear.

The microhardness of coarse-grained material was investigated in [22] and results of microhardness measurement are summarized in Table 7.1. (The resulting values of microhardness, as well as standard deviation were computed from ten indentations).
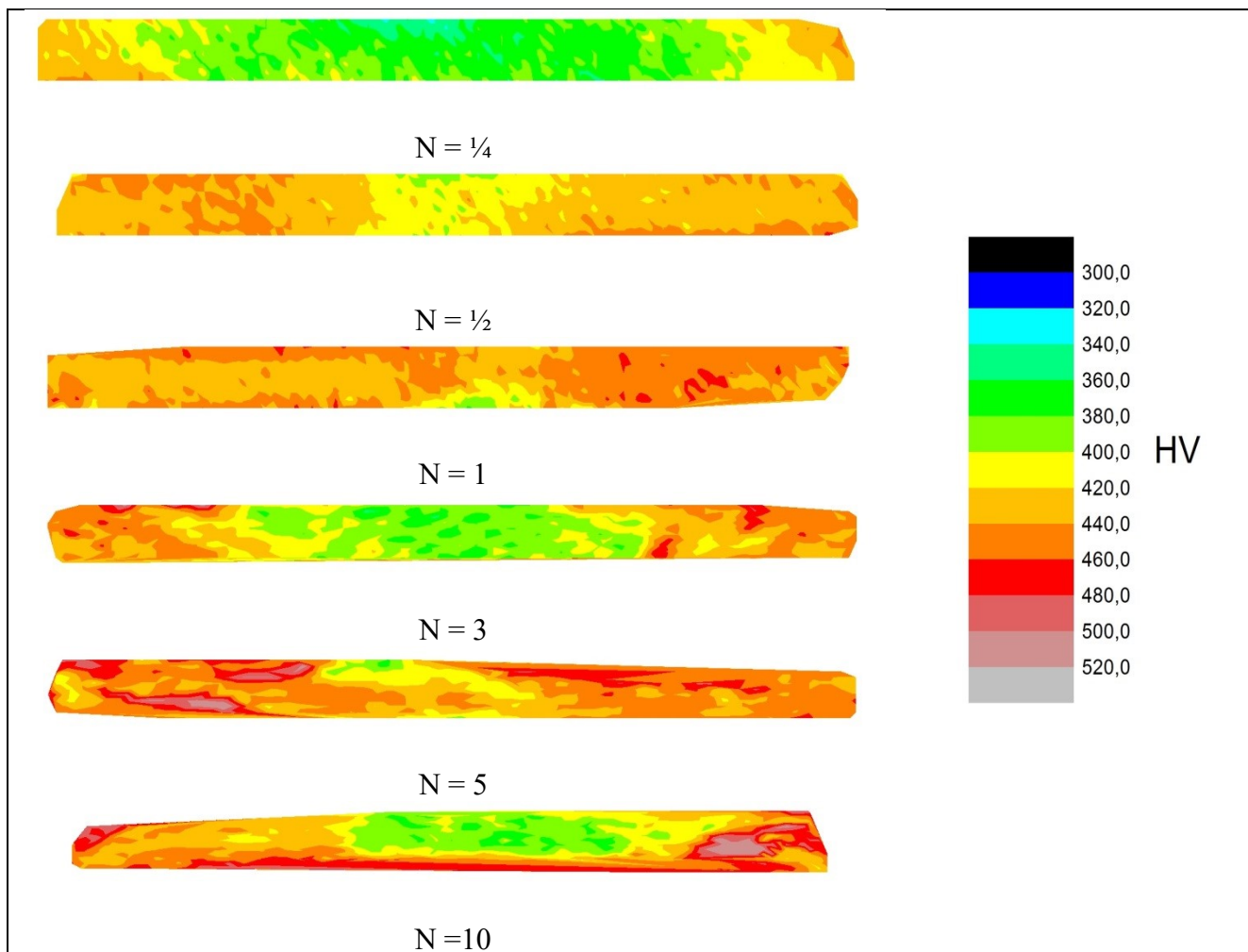
Fig. 7.3. Vickers microhardness of cross-section of Ti-15Mo alloy after HPT process

Sample	HV value ± deviation
Solution treated	278 ± 14
Aged at 573 K for 4 hours	363 ± 6
Aged at 573 K for 16 hours	376 ± 5
Aged at 648 K for 4 hours	464 ± 5
Aged at 648 K for 16 hours	491 ± 6
Heated to 823 K	350 ± 3
Heated to 823 K	293 ± 10

Table 7.1. Microhardness of coarse-grained Ti-15 Mo alloy after different solution treatments [22]

The coarse-grained material can be hardened to HV ≈ 450-500 by appropriate heat treatment. The highest value of strain is obtained by aging treatment at 648 K for 16 hours. The cause of the hardening at 648 K is the formation of the ω-phase particles. The ω-phase particles form obstacles for dislocation movement due to their small size, homogeneous distribution and relatively high volume fraction. At the same time, the material is brittle and cannot be used in a commercial practice. With continuous heating to higher temperatures the material is softened as a result of the dissolution of the ω-phase. Hardening of solution treated material by HPT process does not exceed hardening by ω-phase precipitation even after N = 10 HPT turns.

In the Fig. 7.4. the dependence of the microhardness of samples after various HPT rotations on the equivalent strain by Hencky and von Mises is pointed out. The equivalent strain was calculated from equations (3.2) and (3.3). Decrease of the microhardness around high values of equivalent strain corresponds to the leaking off the material during HPT process, which is not accounted for. Dashed line characterizes the Vickers microhardness of the non-deformed, only solution treated Ti-15Mo alloy (HV ≈ 278) [22].
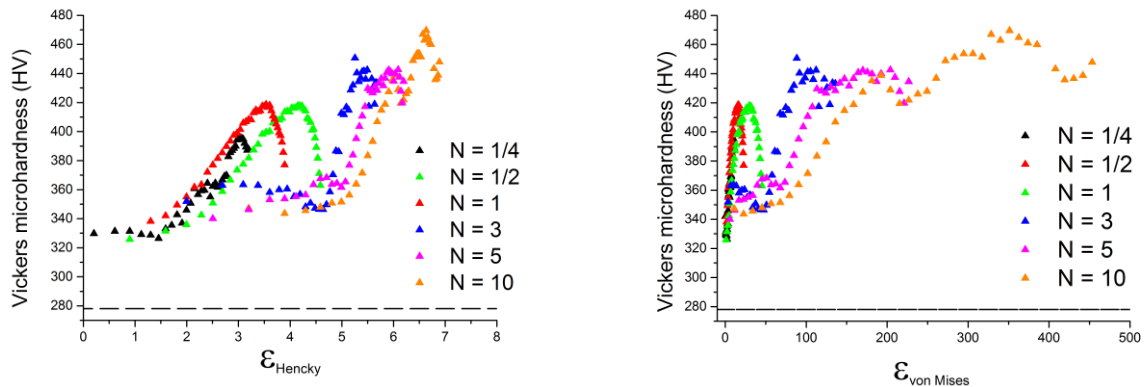

Fig. 7.4. Dependence of the Vickers microhardness of Ti-15Mo alloy on Hencky and von Mises strain (dashed line represents the Vickers microhardness of non-deformed material)

In the study [73] authors claim that three types of variation of hardness exist: strain hardening without recovery, strain hardening with recovery, strain softening. In the case of our sample, strain hardening without recovery is expected.

The Vickers microhardness depending on the von Mises equivalent strain in case of strain hardening follows the equation:

$$HV = K \cdot \varepsilon_{Von\ Mises}^{m} + HV_0, \qquad\qquad (7.1)$$

where *K* is constant, *m* is the hardenability exponent and HV_0 is the microhardness value of non-deformed material.

Microhardness evolution with von Mises strain determined from measurements on all samples does not fall on a single master-curve [74]. This is probably caused by differences between individual samples. For instance, the microhardness in central region is comparatively low and relatively constant. With increasing distance from the sample centre, the microhardness increases suddenly. However, the size of the central region almost stochastically differs between individual samples which are definitely undesirable. Another effect is leaking off of material during HPT causing low microhardness near specimen edge. This effect is not accounted for in strain calculations.

For a better understanding of the hardness evolution a quantitive analysis was conducted for estimating the degree of strain hardening by calculating the hardenability exponent (*m*) which corresponds to the slope in a double-natural logarithmic plot of HV values versus equivalent strain:

$$\ln(HV - HV_0) = lnK + m \cdot ln\varepsilon \qquad\qquad (7.2)$$

This approach for calculating the hardenability exponent was firstly demonstrated on a Ti-6Al-4V alloy after HPT from two different initial conditions and gave hardenability exponent of *0.031* and *0.052* and constant K = *318* and *326,* respectively [75].

In the Fig. 7.5. the microhardness versus von Mises equivalent strain is depicted. In this figure data from measurement of microhardness along the specimen diameter and also from the measurement of cross-section of the sample are shown. Thereby more accurate values can be obtained by fitting and disadvantage of the HPT method that exactly same samples cannot be prepared by HPT process can be partly eliminated. Before fitting this large amount of data were interpolated to 600 equidistant points. Thus the weighted average was taken. Data corresponding to the leaking off the material during HPT process were neglected.
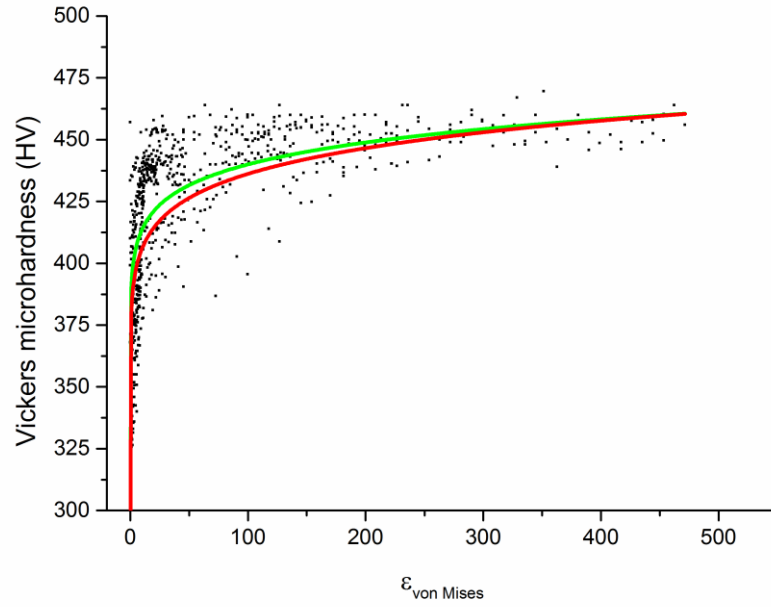
Fig. 7.5. Variation of the measured microhardness values with equivalent strain of Ti-15Mo alloy. The red line denotes the fitted microhardness due to the eq. (7.1), the green line denotes corrected fit.

The fitting of data by eq. (7.1) and calculating of the hardenability exponent was done in two ways. The first was that all data shown in the Fig. 7.5. were fitted; the second was that data which cause the inhomogeneity during HPT process were neglected from fitting (so called corrected fit). The first way of calculation gave the red line in the Fig. 7.5. and second the green line. The red line in the Fig. 7.5. denotes the following form:

$$HV \approx 104 \cdot \varepsilon_{Von\ Mises}^{0.092} + 278 \qquad (7.3)$$

The corrected fit (green line) can be described by the following equation:

$$HV \approx 113 \cdot \varepsilon_{Von\ Mises}^{0.077} + 278 \qquad (7.4)$$

The positive hardenability exponent denotes strain hardening. The hardenability exponent decreases if the fit is corrected. However, it is higher than hardenability exponent of Ti-6Al-4V alloy after HPT process [75]. In comparison with hardenability exponent of ZK60 magnesium alloy after HPT process (*m≈0.07*) or with AZ31 magnesium alloy (*m≈0.08*) the *m* of Ti-15Mo alloy after HPT is also higher or similar [76]. However, in above-mentioned study the hardenability exponent was calculated only from data which correspond to equivalent strain $\varepsilon \in (0; 20)$. Ti-15Mo alloy demonstrates hardening even for very high strains compared

to e.g. Ti-6Al-4V alloy for that the hardening saturates for higher strains leading to lower hardening coefficients.
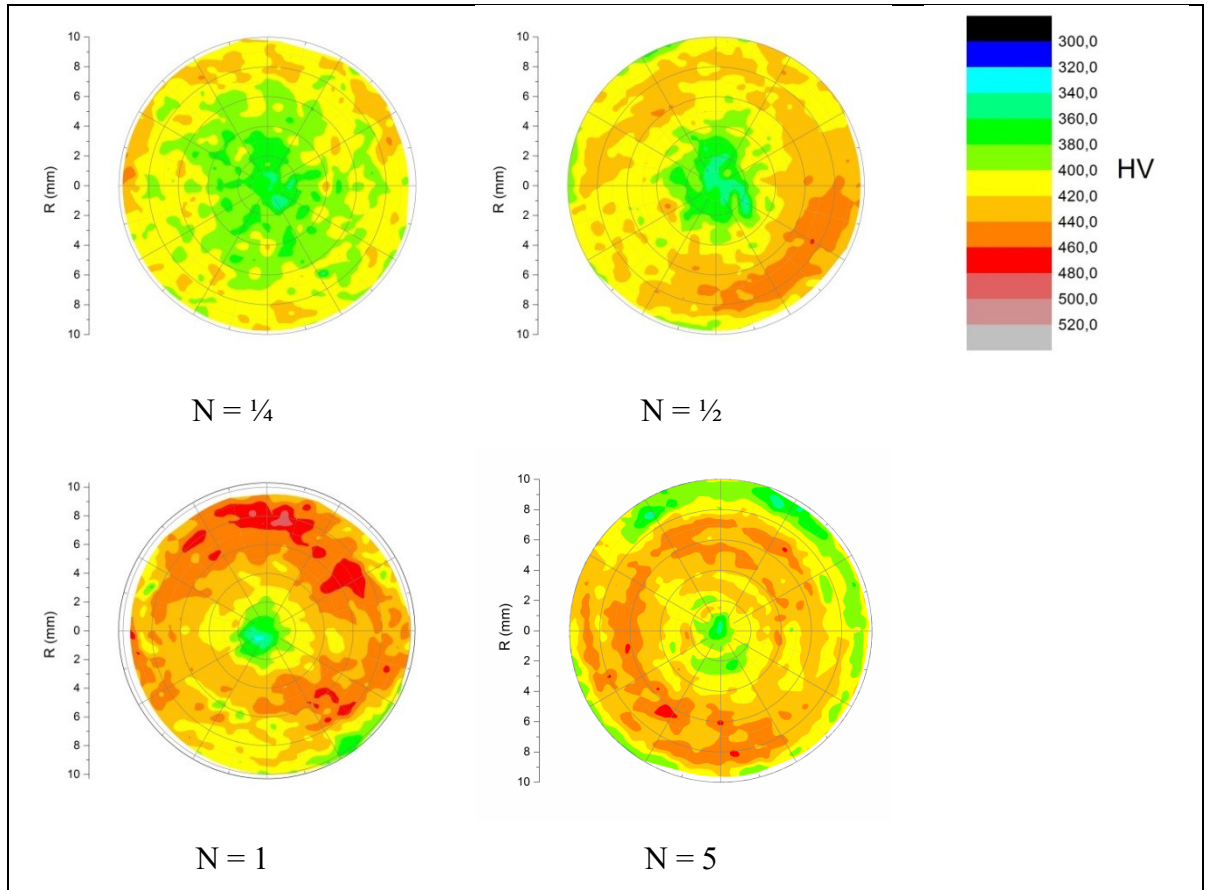
7.1.2. TIMETAL LCB alloy

Fig. 7.6. Microhardness of TIMETAL LCB alloy after various number of HPT turns represented on colour-coded polar diagram

In the Fig. 7.6. the Vickers microhardness of TIMETAL LCB alloy after N = ¼, ½, 1 and 5 HPT turns is represented . The microhardness generally increases with the number of HPT turns and also with increasing distance from the centre of the specimen. The inhomogeneity of microhardness can be observed; however, in contrast with Ti-15Mo alloy, with increasing number of HPT rotations the microhardness becomes more homogenous. In the Fig. 7.7. the radial dependence of Vickers microhardness is shown. The increasing microhardness with increasing distance from the centre of the specimen and with increasing number of HPT rotations is observed. Nevertheless, on the peripheral region decreasing of the microhardness is visible thanks to the leaking off the material during high pressure

torsion. The lowest HV value of microhardness is in the centre of the sample (HV ≈ 350), the maximum value is around 450 HV. In contrast to the Ti-15Mo alloy values of Vickers microhardness are comparable but the increase of the microhardness with the distance from the centre of the specimen is more homogeneous in the case of TIMETAL LCB alloy.
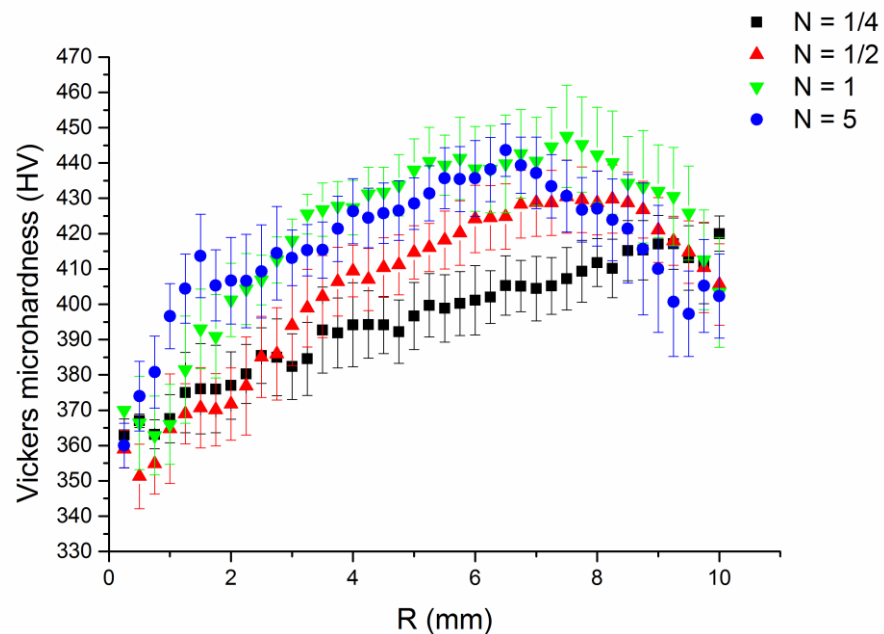

Fig. 7.7. Radial dependence of Vickers microhardness of TIMETAL LCB alloys for various HPT rotations

Fig. 7.8. depicts the Vickers microhardness of cross-section of TIMETAL LCB alloy. The increase of the microhardness with increasing number of HPT rotations is evident such as the increase of microhardness with increasing distance from the centre of the specimen. In comparison with microhardness measurement on the whole discs, the microhardness of the cross-section of the specimen is higher. This difference may be caused by preparation of the individual samples by HPT method.. In contrast to the Ti-15Mo alloy the microhardness is higher on the rim of the sample and more homogenous.
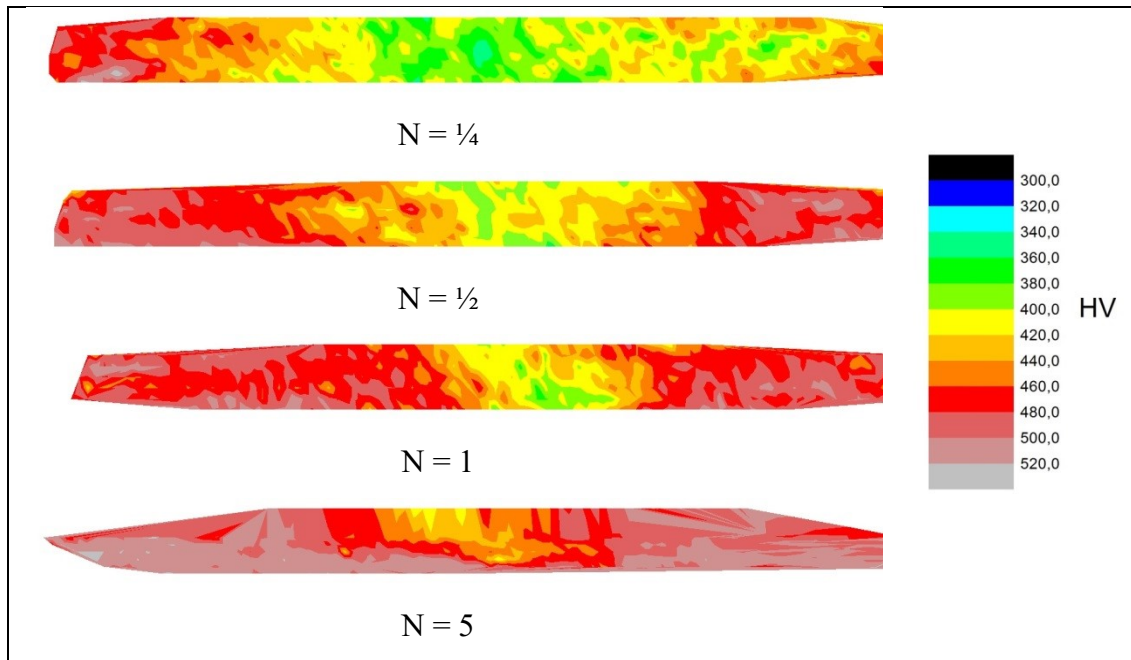
Fig. 7.8. Vickers microhardness of cross-section of TIMETAL LCB alloy after HPT process

The microhardness of the coarse-grained TIMETAL LCB alloy was studied in [57]. In the Table 7.2. the results of the microhardness of coarse-grained material after ageing at various temperatures for various time are summarized. (The resulting values of microhardness, as well as standard deviation were computed from ten indentations).

In comparison with coarse-grained material, the HV value of the microhardness higher than HV ≈ 500 can be reached with appropriate heat treatment. The reason is analogous as in the case of Ti-15Mo alloy and corresponds to the formation of the ω-phase and consequent ω→α transformation. A similar microhardness can be achieved by HPT of solution treated material as in the case of aged α+β condition. The microhardness after HPT process is, however, lower than for β+ω condition.

In the Fig. 7.9., dependences of the microhardness of samples after various HPT rotations on the equivalent strain by Hencky and von Mises are shown. The equivalent strain was calculated from equations (3.2) and (3.3). The decrease of the microhardness around a high value of equivalent strains corresponds to the leaking off the material during HPT process, which is not accounted for. Dashed line symbolizes the Vickers microhardness of the non-deformed solution treated TIMETAL LCB alloy (HV≈ 343) [57].

42

Sample	HV value ± deviation
Solution treated	343.0 ± 3.6
Aged at 673 K for 4 hours	510.0 ± 3.5
Aged at 673 K for 256 hours	556.7 ± 4.1
Aged at 723 K for 4 hours	550.7 ± 5.0
Aged at 723 K for 256 hours	505.9 ± 6.2
Aged at 773 K for 4 hours	491.7 ± 4.6
Aged at 773 K for 256 hours	449.8 ± 2.8

Table 7.2. Microhardness of coarse-grained TIMETAL LCB alloy after different solution treatments [57]
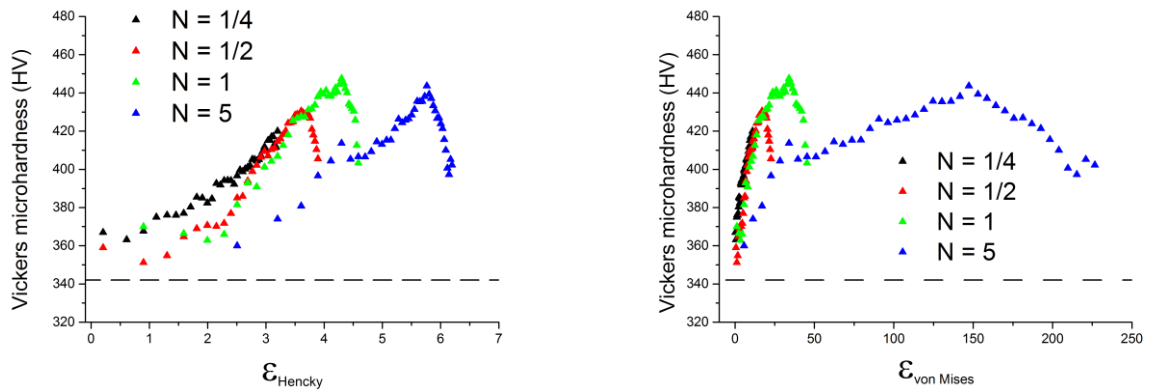

Fig. 7.9. Dependence of Vickers microhardness of TIMETAL LCB alloy on Hencky and von Mises strain

The quantitative analysis and calculating of the hardenability exponent was done analogously than in case of Ti-15Mo alloy.

The red line in the Fig. 10. denotes the following equation:

$$HV \approx 68 \cdot \varepsilon_{Von\,Mises}^{0.154} + 343 \tag{7.5}$$

The corrected fit (green line) can be described by the following form:

$$HV \approx 68 \cdot \varepsilon_{Von\,Mises}^{0.173} + 343 \tag{7.6}$$

The results show that hardenability exponent of TIMETAL LCB alloy is higher than hardenability exponent of Ti-15Mo alloy.
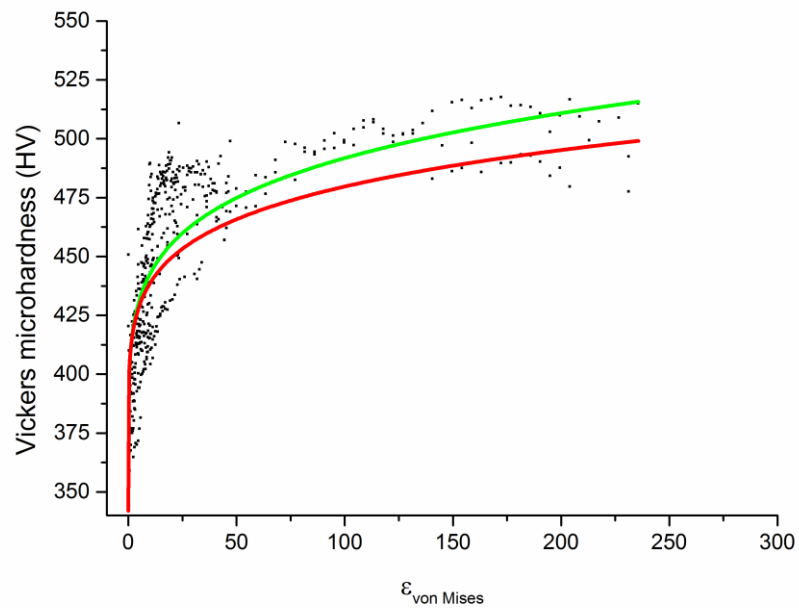
Fig. 7.10. Variation of the measured microhardness values with equivalent strain of TIMETAL LCB alloy. The red line denotes the fitted microhardness due to the eq. (7.1), the green line the corrected fit.

7.2. Microstructure after HPT

Scanning electron microscopy was used for investigation of microstructure of samples deformed by HPT after various numbers of turns. For SEM observations the same samples as for microhardness measurement over whole disc were used. In the Fig. 7.11., the method of the observation by SEM is schematically illustrated.
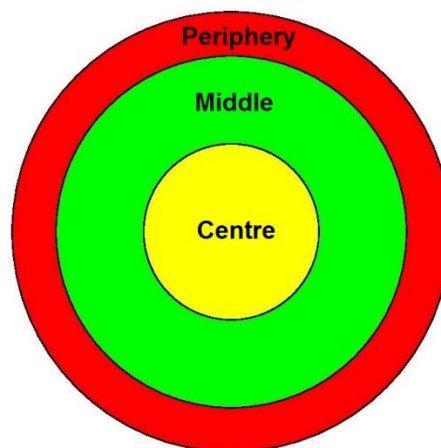

Fig. 7.11. Observation schematic illustration (scheme prepared by AutoCAD)

7.2.1. Ti-15Mo alloy

In the Fig. 7.12. the microstructure of Ti-15Mo alloy after ¼ HPT turns is shown. The contrast in figures is given by channelling contrast. Thus grains with different orientation can be partly distinguished. The increasing deformation with the distance from the centre of the specimen is demonstrated. Bigger (~20 µm) heavily deformed grains occur in the centre part. The grain size decreases with increasing deformation (i.e. distance form specimen centre) and in the middle part, small grains between bigger grains can be seen. On the periphery, ultra-fine grain structure appears.

The microstructure of central part of the specimen was studied also by EBSD measurement. Fig. 7.13. shows inverse pole figure map from the centre part of the Ti-15Mo alloy after ¼ HPT turns. In the image, each point is coloured according to the crystallographic orientation. Relation between colouring and orientation is given by orientation triangle shown in the bottom right corner of the EBSD image. Moreover, high- and low-angle grain boundaries are also highlighted by black and red colour, respectively. The microstructure consists of large grains, which are heavily deformed and lattice rotation within grains is observable. Many grains are severely twinned. Fragmentation of microstructure and UFG structure formation is visible mainly in the top right corner.

We selected one grain from inverse pole figure map depicted in Fig. 7.13. and its detail is provided in the Fig. 7.14. The lattice rotation within one grain can be observed after only ¼ HPT turn and is quantified by the point-to-origin misorientation of the grain depending on the distance from the origin (beginning of the black line). It shows that the misorientation within grain increases up to 10° which suggests a high degree of the deformation. Approximately in the distance of 42 µm and 55 µm from the selected origin, the point-to-point misorientation is abruptly increased which corresponds to the low-angle grain boundary or subgrain boundary between those newly created grains/subgrains. The deformation within the new grains/subgrains is also visible.
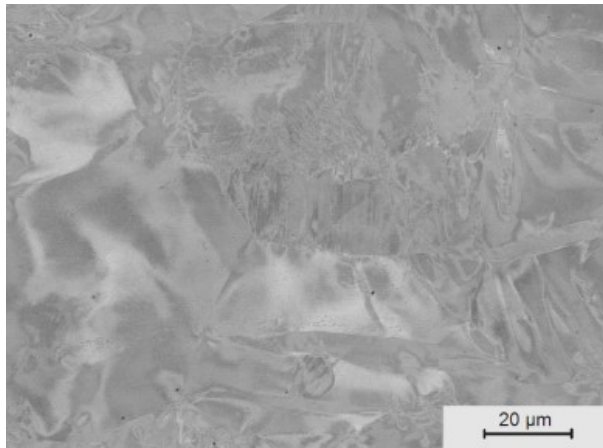
Centre
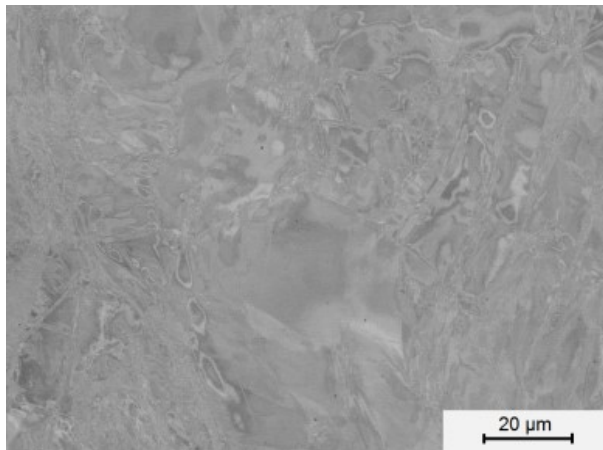
Middle
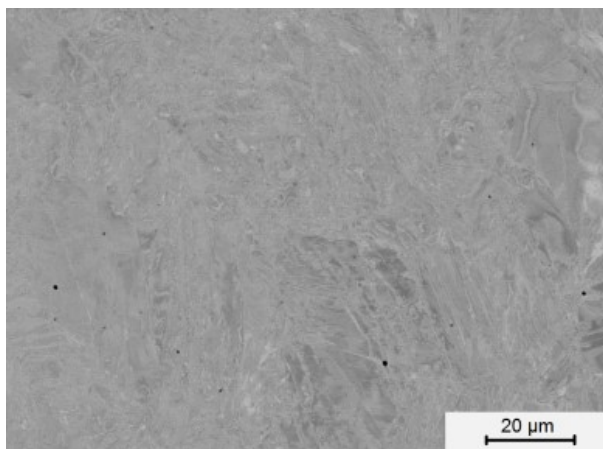
Periphery

Fig.7.12. SEM image of Ti-15Mo alloy after ¼ HPT turns
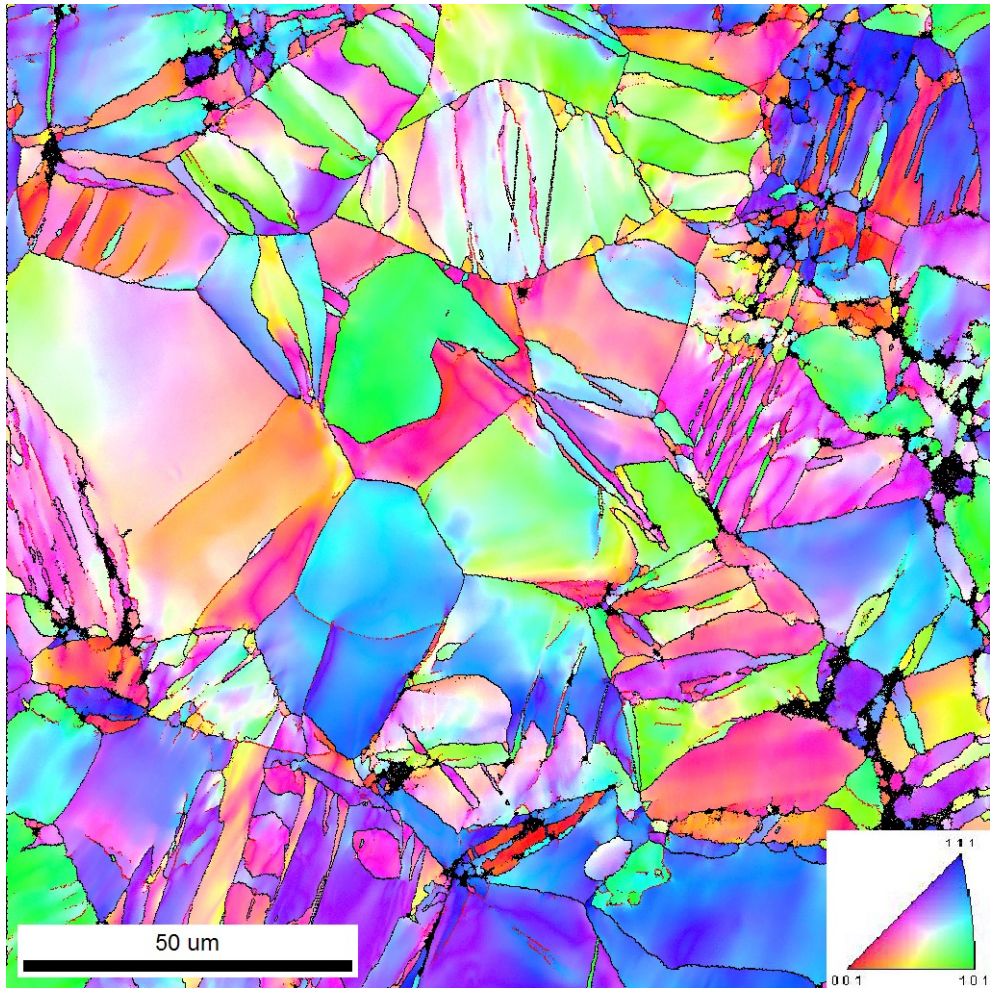
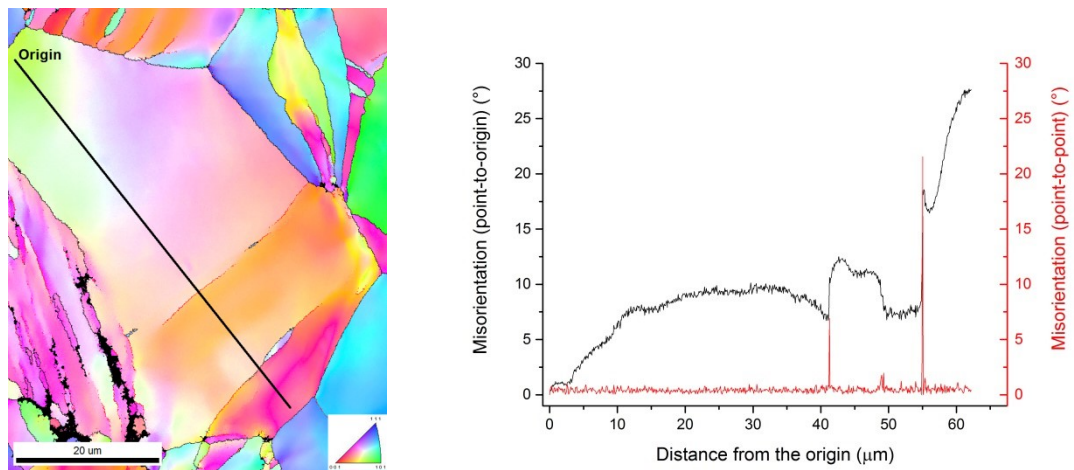Fig. 7.13. Inverse pole map figure from the centre part of the Ti-15Mo alloy after ¼ HPT turns

Fig. 7.14. Inverse pole map figure of heavily deformed grain and dependence of the misorientation along the highlighted black line
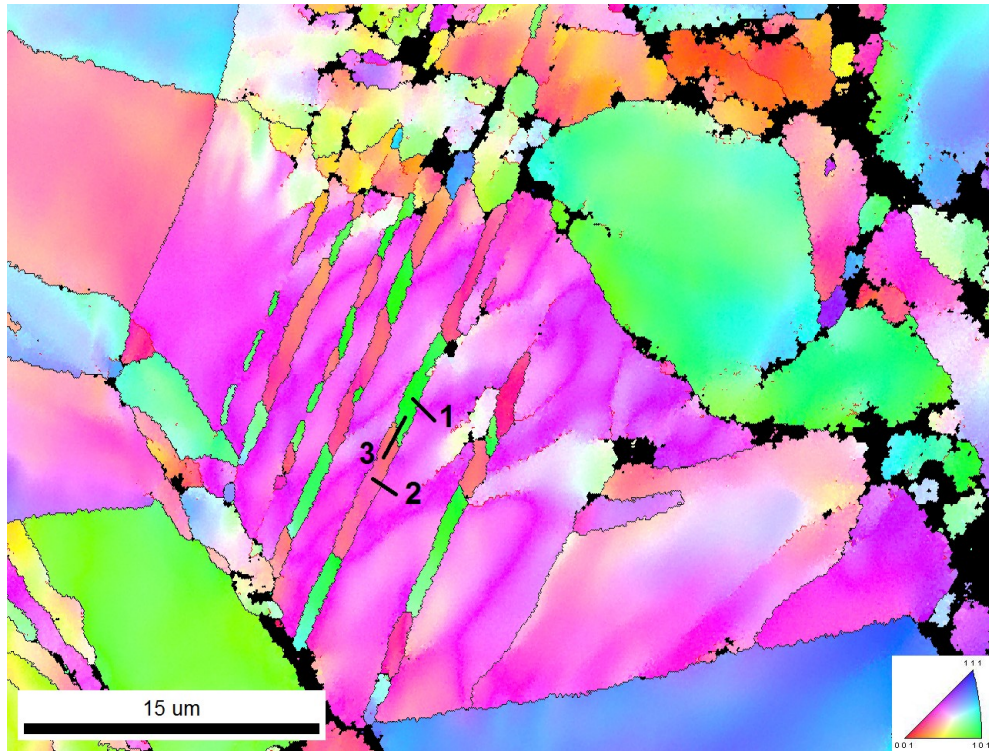
Fig. 7.15. Inverse pole map figure of twinned grain of Ti-15Mo alloy after N = ¼ HPT turns

Another selection from the IPF map in the Fig. 7.13. is the twinned grain shown in detail in the Fig. 7.15. Different colours inside twins suggest the secondary twinning procedure. The original grain (purple colour) is also severely deformed. We measured the point-to-origin and point-to-point misorientations along the highlighted black lines in the Fig. 7.15. The misorientations were evaluated between the matrix and twins (marked as 1, 2) and between two twins (marked as 3). The origin of the black lines is denoted by a number. The highest value of the point-to-origin in the first case (1) is around 40°. In the second case (2), the highest value of point-to-origin misorientation is ~57°. Similar value was obtained for the misorientation between the two twins (3). Based on these results the twinning system(s) in Ti-15Mo alloy were studied.
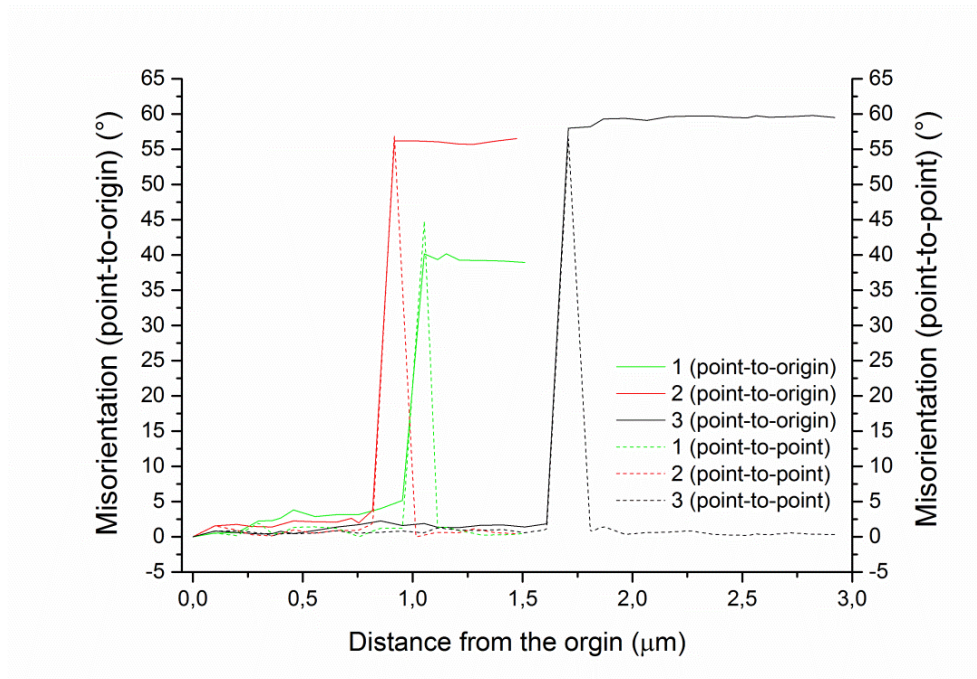
Fig. 7.16. Misorientation along the highlighted black lines in the Fig. 7.15.

It is well known that the {1 1 2} ⟨1 1 1⟩ mechanical twining is one of the most important mode of plastic deformation in body-centered cubic (BCC) metals and alloys, especially at low temperatures and at high strain rates [77-80]. The zig-zag shape of the {1 1 2} ⟨1 1 1⟩ twins in metastable β-Ti alloys was investigated by Yang et al. [81] and by Li et al. [82]. Other type of twinning system in β-Ti alloys (BCC crystals) is {3 3 2} ⟨1 1 3⟩ [83, 84]. The twinning system selection was studied in [85].

In the Fig. 7.17. the selected part from the Fig. 7.13. is represented. In this figure matrix and twins are clearly separated. The crystallographic orientations of the matrix and the twin (purple colour) are shown. In order to determine the twinning system between matrix and twins software Mathematica was used. From the graphic representation it is clearly visible that twinning occur relative to the plane {1 1 2}.
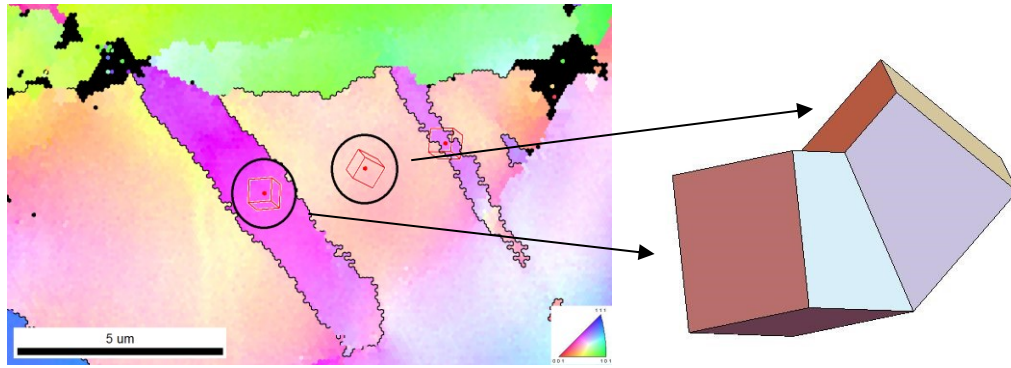
Fig. 7.17. Left figure: Inverse pole map figure of Ti-15Mo alloy after N = ¼ HPT turns. The orientation of the matrix (pink) and twins (purple) are indicated. Right figure: Graphical representation of the twinning system between matrix and twins.
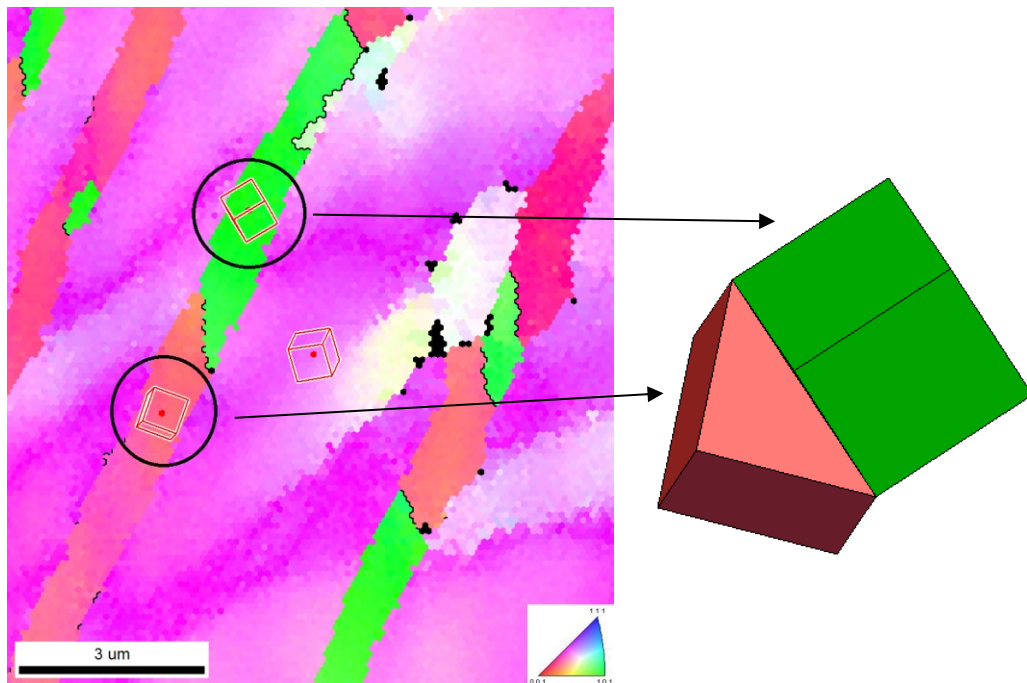
Fig. 7.18. Left figure: Inverse pole map figure of Ti-15Mo alloy after N = ¼ HPT turns. The orientation of the matrix (purple) and twins (red and green, respectively) are indicated. Right figure: Graphical representation of the twinning system between two twins.

Afterwards, the twinning system between two twins (red and green) was also investigated. In the Fig. 7.18. the twinning structure of the Ti-15Mo alloy after N = ¼ HPT rotations is visible. The orientations of the matrix and twins are again schematically shown. The orientations between matrix and the twin and between two twins are graphically represented Fig. 7.18. The twinning plane is again {1 1 2}.

The twinning system {1 1 2} 〈1 1 1〉 is clearly documented. Moreover it is clear that the primary twins undergo secondary twinning. It can be concluded that multiple mechanical twinning significantly contributes to the grain fragmentation and microstructure refinement.

EBSD images from materials with higher equivalent strain are not available due to ultra-fine and heavily deformed microstructure which disallows successful collecting of Kikuchi diffractograms.

7.2.2. TIMETAL LCB alloy

In the Fig. 7.19. the microstructure of TIMETAL LCB alloy after ¼ HPT turns is depicted. The contrast between each area in the figure is again given by channelling contrast. The increasing deformation with the distance fr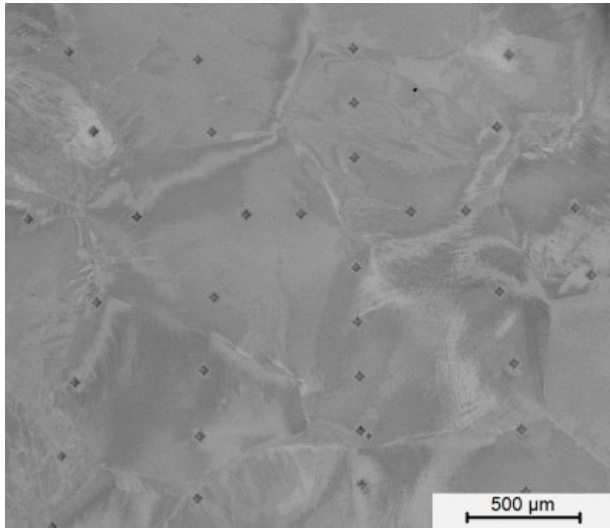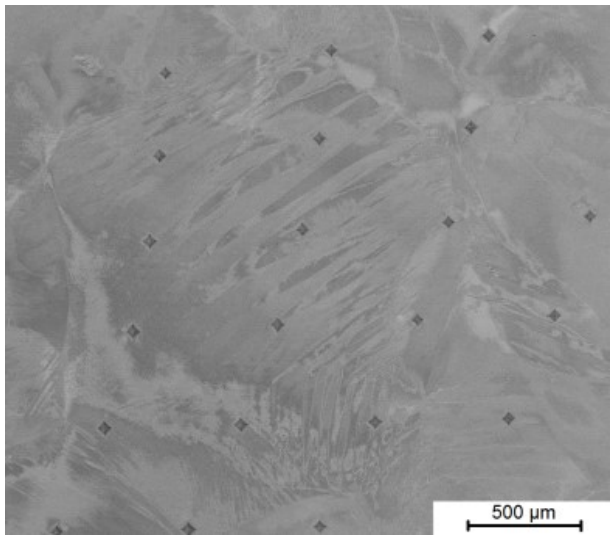om the centre of the specimen is shown, but the microstructure refinement is much lower than that of Ti-15Mo alloy, which might be also caused by significantly coarser initial microstructure. In the centre part, big (almost 1 mm) grains occur. These grains are deformed but not fragmented. The grain size slightly decreases with increasing distance from the centre of the specimen and in the middle part bigger grains are probably surrounded by small grains. The microstructure is clearly heavily twinned. On the periphery, grains are not clearly distinguishable due to their small size. Lighter bands are also observed on the micrograph. These might be associated with deformation bands or even with β-stabilizer enhanced areas as suggested in [84, 86], though we are not aware of any mechanism, which may cause such element segregation. The microstructure of TIMETAL LCB alloy after ¼ HPT turns correspond to the microhardness measurement; the deformation is heterogeneous, it is lower in the centre part and increases along the radius of the sample.

In the Fig. 7.20. and Fig. 7.21., inverse pole figure maps of the TIMETAL LCB alloy after ¼ HPT rotations are shown. In the Fig. 7.20. the centre part of the sample is depicted. The green cross in the centre of the sample represents the centre of the specimen as specified by microhardness measurement. In the EBSD image, indents of microhardness measurement are clearly visible. Grains in the centre of the specimen are large and the deformation degree is not as high as in the case of Ti-15Mo alloy.

Centre

Middle
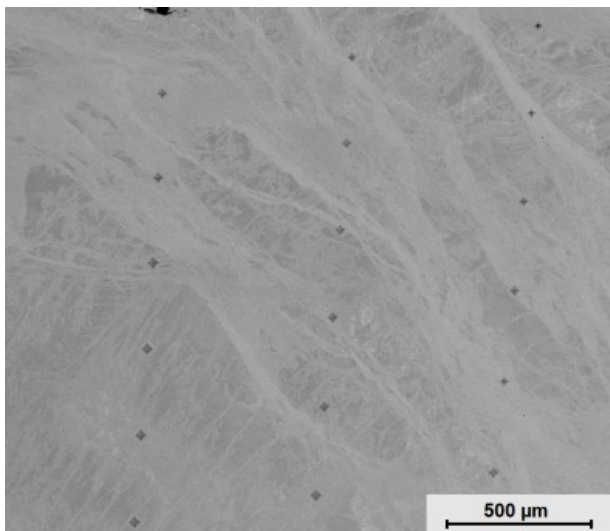
Periphery

Fig.7.19. SEM image of TIMETAL LCB alloy after ¼ HPT turns

In the Fig. 7.21. the middle part of the specimen is shown. The deformation increased as compared to the centre part. Increased lattice rotation and twinning within grains are observable. In the lower right corner of the EBSD image twins and twinning-induced grain refinement are clearly visible. Twinning-induced grain refinement was also described for magnesium alloys (HCP) [87, 88], stainless steel (FCC) [89] in copper (FCC) [90] and for commercially pure titanium (HCP) [91].
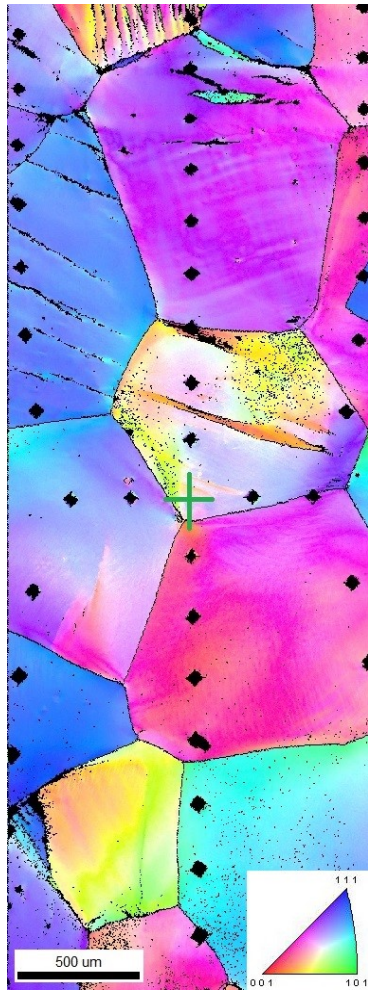
Fig.7.20. Inverse pole map figure of TIMETAL LCB alloy after ¼ HPT turns (centre part)
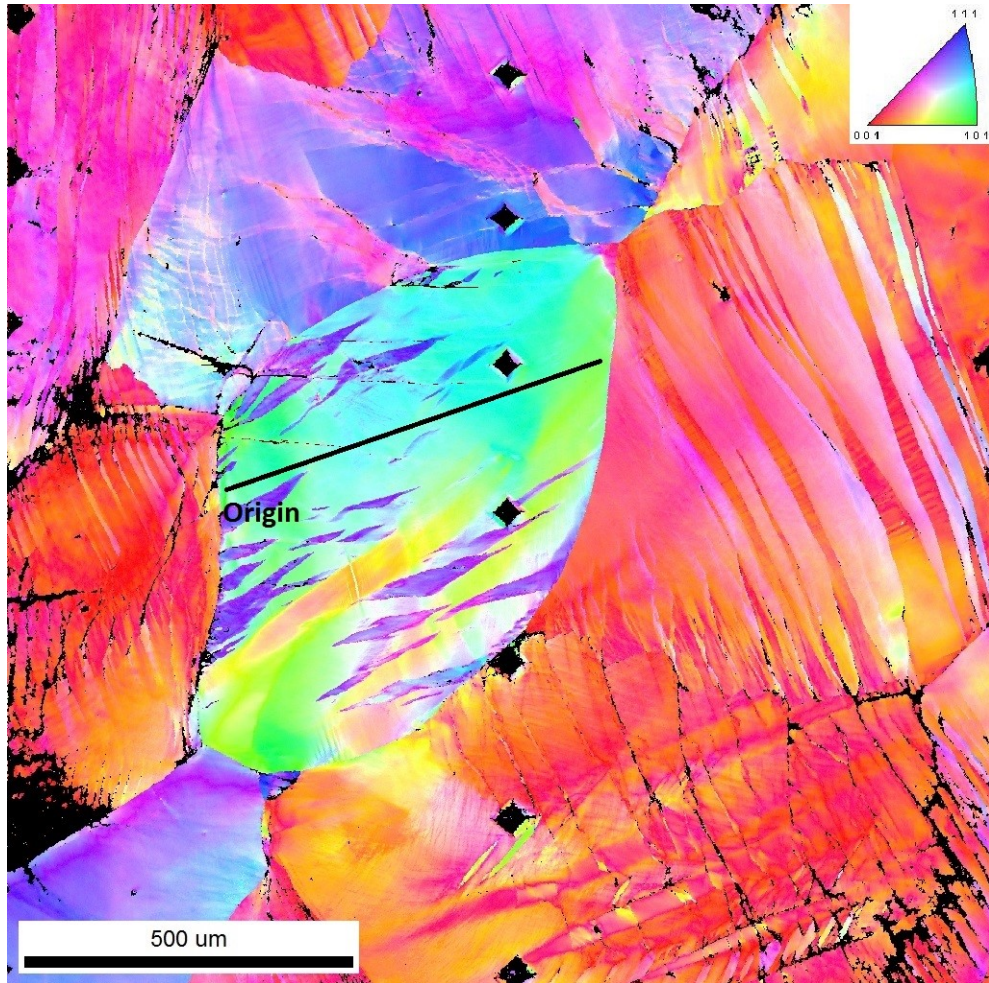
Fig. 7.21. Inverse pole map figure of TIMETAL LCB alloy after ¼ HPT turns (middle part)

The noticeable grain in the middle of image in the Fig. 7.21. was selected for estimation of the deformation along the grain diameter. The point-to-origin misorientation of grain depending on the distance from the origin (beginning of the black line) shows that the misorientation within grain reaches 10° which suggests high degree of the deformation within single grain. Along the examined line, subgrain boundaries cannot be found (no sudden increase in point-to-point misorientation exceeding 5°).

Nevertheless, stress concentrations, twinning-induced deformation and twinning-induced microstructure fragmentation are noticeable in the EBSD map.
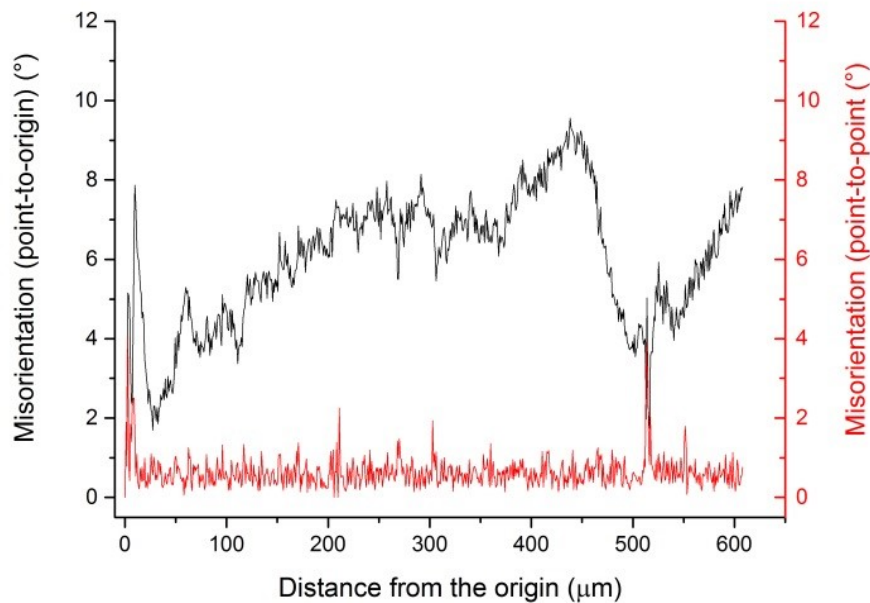
Fig. 7.21. Inverse pole map figure of heavily deformed grain and dependence of the misorientation along the highlighted black line

Comparison of Ti-15Mo and TIMETAL LCB alloys

The two investigated alloys, Ti-15Mo and TIMETAL LCB alloy based on the results of the microhardness measurements and scanning electron microscopy observations can be compared.

In Ti-15Mo alloy the microstructure is more fragmented after ¼ HPT turn than in TIMETAL LCB alloy. It might be caused by coarser initial microstructure or slower microstructure fragmentation in TIMETAL LCB. In both alloys, twinning-induced fragmentation seems to be the dominant mechanisms in the initial stage of deformation by high pressure torsion. Microhardness of Ti-15Mo and TIMETAL LCB metastable β-Ti alloys increases with increasing number of HPT rotations and also with increasing distance from the centre of the sample. By comparing microhardness of HPT deformed condition with coarse-grained conditions after β solution treatment we found that microhardness increase after HPT is higher in Ti-15Mo alloy than in TIMETAL LCB alloy. This might be caused by the fact that TIMETAL LCB alloy is more solution strengthened in coarse-grained condition or that the microstructure refinement is more efficient in Ti-15Mo alloy.

The highest microhardness after HPT exceeds significantly the microhardness of two phase α + β heat-treated material in both alloys.

7.3. Defect structure of Ti-15Mo alloy

The defect structure of the Ti-15Mo alloy deformed by high pressure torsion after N= 3, 5 and 10 rotations was investigated by positron annihilation spectroscopy (PAS). To reflect the two regions with different microhardness and microstructure, the positron lifetime measurements were performed at the centre ($r = 0$ mm) and also on the periphery ($r = 7$ mm) of the sample (see Fig. 7.11.).

7.3.1. Reference samples

Reference sample for this measurement was pure Ti. The well-annealed pure Ti shows a single component lifetime spectrum with a lifetime of $\tau_B = (144.6 \pm 0.5)$ ps which is consistent with the calculated bulk lifetime for Ti [69]. The defect density in the well annealed Ti is very low (below PAS sensitivity limit) and samples can be considered as virtually defect-free materials. The lifetime spectra of pure Ti after deformation by HPT [56] can be well fitted by a single component with lifetime of (176 ± 1) ps, which is slightly shorter than the lifetimes calculated for single vacancies in Ti [69]. Such lifetime is typical for dislocations [92]. Thus the component can be attributed to positrons trapped at dislocations introduced by severe plastic deformation. Therefore, HPT deformed pure Ti demonstrates very high density of dislocations. Practically all positrons in these samples are annihilated in trapped state at dislocations, an effect known as saturated positron trapping [71]. The free positron component cannot be determined in lifetime spectrum when its intensity falls below $\approx$ 5%. From the defect-free reference sample can be computed the S_0 and W_0 parameter and from deformed reference sample the component corresponding to the dislocations of the S and W parameter (S_D, W_D).

7.3.2. Ti-15Mo alloy after deformation by HPT

The positron lifetime spectra of Ti-15Mo samples after HPT (N = 3, 5, 10) can be well fitted by two components. The shorter component with lifetime $\tau_1 < \tau_B$ represents a contribution of free positrons while the longer component with lifetime τ_2 comes from positrons trapped at defects. The lifetime of $\tau_2 \approx 175$ ps of the latter

component is consistent with the lifetime measured in pure Ti deformed by HPT and can be attributed to positrons trapped at dislocations created by severe plastic deformation during HPT processing. The development of lifetimes τ_1, τ_2 and the intensity I_2 of positrons trapped at dislocations with increasing number of HPT revolutions for centre and periphery of each sample is plotted in Fig. 7.22. (a) and (b), respectively.
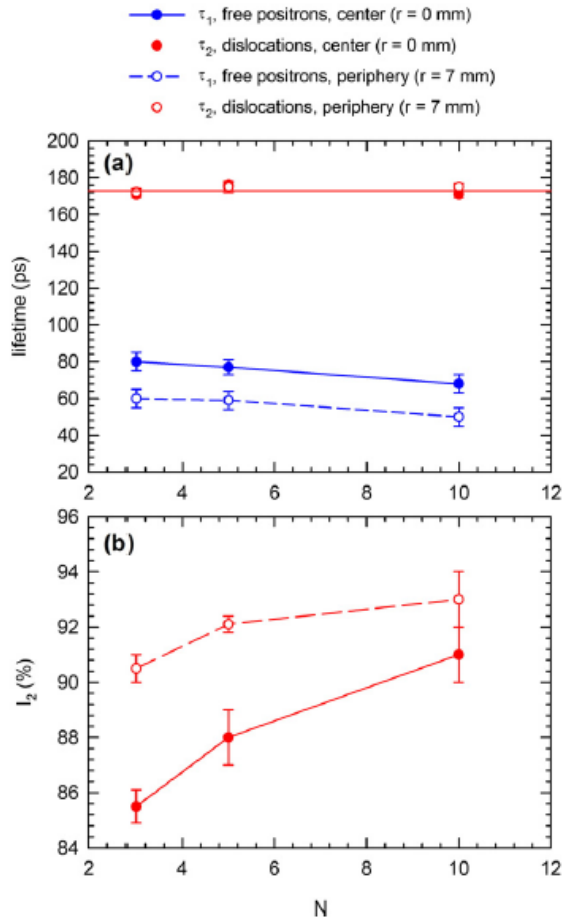
Fig. 7.22. Dependence of the (a) positron lifetimes and (b) the intensity I_2 of positrons trapped at dislocations on the number of HPT revolutions N of Ti-15Mo alloy after deformation by HPT

The lifetime τ_2 is approximately constant which means that nature of defects, i.e. dislocations, remains unchanged. The intensity I_2 (Fig. 7.22. b.)) increases with the number of HPT revolutions. This proves that the dislocation density increases during HPT processing. Concurrently, the lifetime τ_1 decreases, because statistically it is more likely that positrons with shorter lifetimes annihilate as free positrons and positrons with longer lifetimes are trapped at defects. In addition, Fig. 7.22. b)

57

depicts that the contribution of positrons trapped at dislocations in the centre of the sample in each case is lower than at the periphery of the sample disc. This is caused by non-uniform shear strain imposed on the sample disc during HPT processing [93].

The Doppler broadening (DB) investigations were performed at various distances from the centre of the sample. The positron source spot was placed at various distances from the centre of the sample using a micrometer x–y shift. The uncertainty in the position of the positron source was ~0.1 mm. The dependence of the S parameter on the distance from the centre of the specimen Ti-15Mo alloy deformed by HPT is plotted in Fig. 7.23.
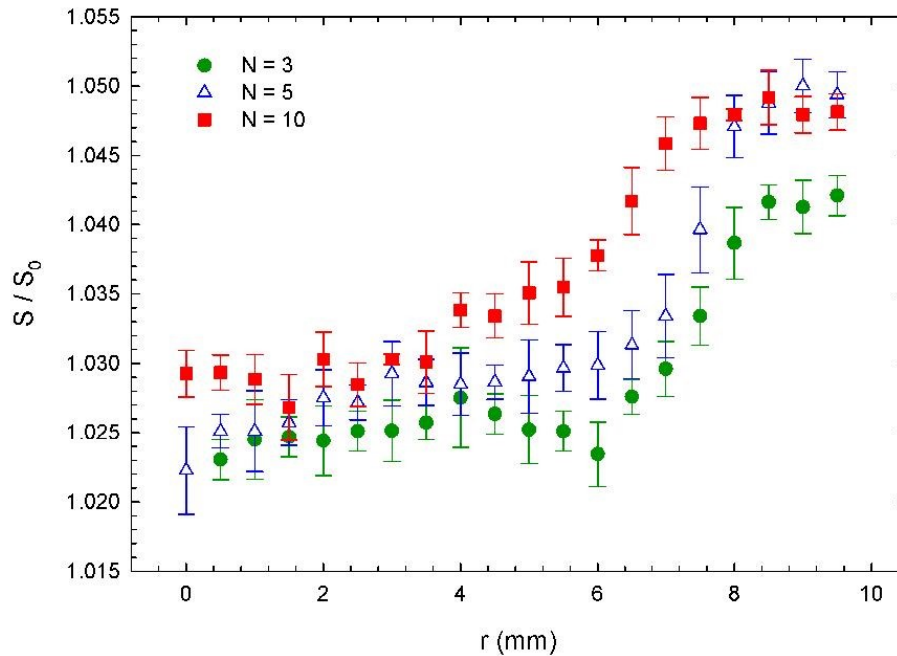
Fig. 7.23. Dependence of the S parameter on the distance from the centre of the sample of Ti-15Mo alloy deformed by HPT

Up to $r \approx 4$–5 mm the S parameter only slightly increases while at larger distances from the centre S exhibits a pronounced increase. Thus, two regions of the sample can be distinguished:

(i)   a central part characterized by lower density of dislocations and

(ii)   a peripheral region with higher dislocation density which increases with the distance from the centre of the specimen.

This is in accordance with microhardness studies (see Fig. 7.1., Fig. 7.2 and Fig. 7.3.) which showed a distinct difference between the central part with lower

strain and hardness and the peripheral region with remarkably higher hardness. The evolution of the S parameter with increasing number of HPT turns exhibits some differences compared to the radial dependence of the microhardness (Fig. 7.2). While S parameter increases with number of HPT revolutions, microhardness saturates at the periphery already for the sample N = 3. In the region closer to the centre, microhardness increases with increasing number of HPT turns and becomes saturated for the specimen N = 5. Finally, microhardness in the centre is comparable for all samples. These differences between the development of the S parameter and the microhardness can be caused by some factors:

(i) PAS and microhardness measurement were carried out on different samples.

(ii) Microhardness may saturate at lower dislocation density than the S parameter.

The correlation plot of the S and W parameters (S-W plot) is shown in Fig.7.24. It is noticeable that points measured for Ti-15Mo alloy lie along a straight line connecting the point $[W_0, S_0]$ for the annealed Ti, where practically all positrons annihilate in the free state, and the point $[W_D, S_D]$ for Ti after deformation by HPT which exhibits saturated positron trapping at dislocations. This behaviour gives clear evidence that positrons in Ti-15Mo alloy after HPT deformation are trapped in dislocations and that the nature of these defects does not change with increasing deformation. Only the defect density varies across the sample disc and increases with the number of HPT revolutions.
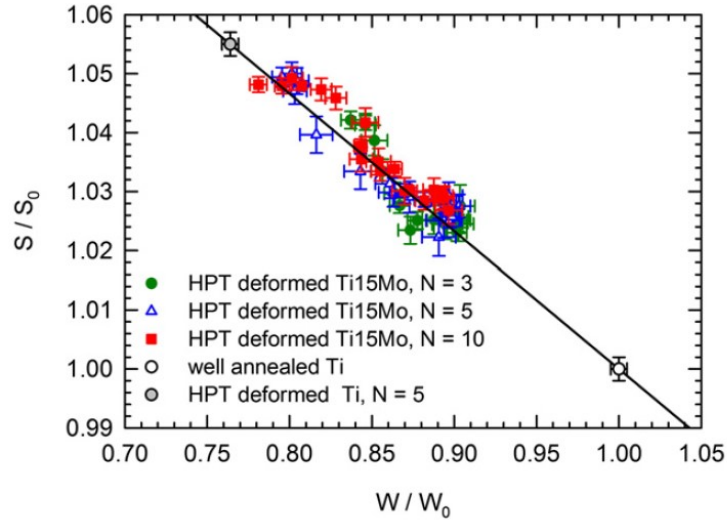
Fig. 7.24. The S–W plot for HPT deformed Ti-15Mo alloy. The solid line connects the points for the well annealed pure Ti (virtually defect free material) and HPT deformed pure Ti (saturated trapping at dislocations).

7.3.3. Determination of dislocation density

Fig. 7.25. depicts dislocation densities calculated from DB data by equation (5.11) and from lifetime results by equations (5.7) and (5.8). The dislocation density in the central region falls into the range $(1–2) \times 10^{14}$ m^{-2} while in the periphery ρ_D rises remarkably and approaches 10^{15} m^{-2} in the periphery of samples subjected to 5 and 10 HPT revolutions. Note that Ti-15Mo alloy after HPT deformation exhibits lower density of dislocations than Ti-6Al-7Nb alloy after HPT deformation [33] where ρ_D in the centre becomes $\approx 3 \times 10^{14}$ m^{-2} while at the periphery ρ_D increased up to 5×10^{14} m^{-2} already after the first quarter of HPT revolution (N=¼). With further HPT straining N > ½ the dislocation density exceeds 10^{15} m^{-2} leading to saturated positron trapping [94]. Contrary to HPT deformed Ti-6Al-7Nb alloy which shows uniform microstructure across the whole sample disc already after the N ≥ ½ of HPT revolution the Ti-15Mo sample exhibits non-uniform density of dislocations across the sample disc even after 10 HPT revolutions. Another important difference is that Ti-6Al-7Nb alloy after HPT deformation contains vacancy clusters formed by agglomeration of deformation-induced vacancies while no vacancy clusters were observed in Ti-15Mo alloy. This could be associated with higher production rate of vacancies in Ti-6Al-7Nb consisting of a mixture of HCP α-phase and BCC β-phase compared to Ti-15Mo alloy which has BCC structure. The dislocation climbing,

60

which is known to introduce vacancies, can be expected to occur more frequently in HCP structure with a smaller number of active slip systems.

Results of the positron lifetime measurement and Doppler broadening are consistent with results of the microhardness measurement. It means that dislocation density which causes the strengthening of the material increases with the distance from the centre of the sample and with number of HPT revolutions, respectively.
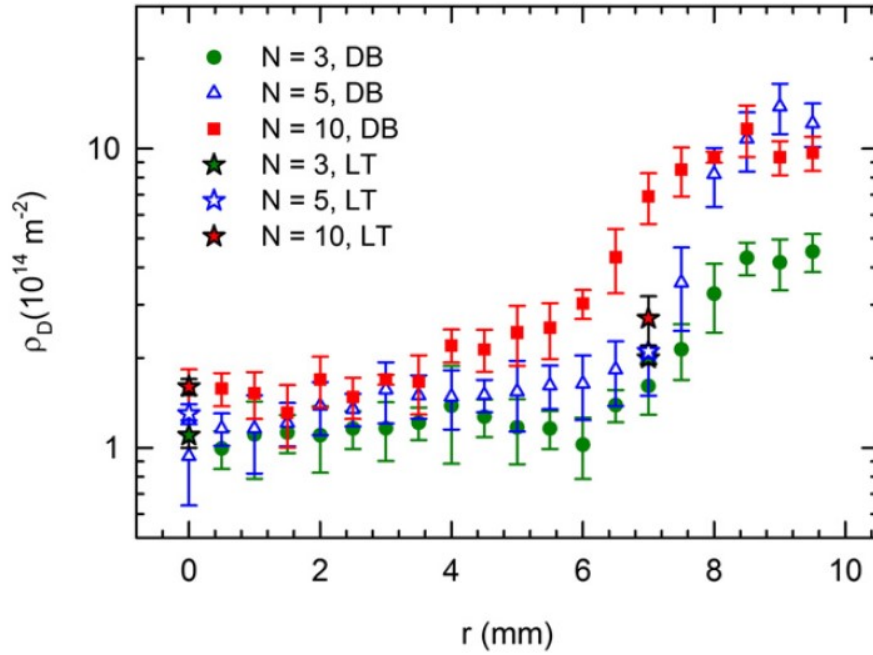
Fig. 7.25. Dislocation densities for HPT samples of Ti-15Mo alloy calculated from lifetime and DB results and plotted as function of the distance from the centre of the sample

7.4. Differential scanning calorimetry

Subsequent annealing \ Deformation	Deformed by HPT	Non-deformed
None	2 samples	2 samples
up to 823 K (5 K/min)	2 samples	2 samples
up to 843 K (5 K/min)	2 samples	2 samples

Table 7.3. Number of investigated samples per condition for DSC measurement

Selected samples of Ti-15Mo alloy were observed by DSC measurements. In the Table 7.3. the conditions of the investigation are summarized. Two samples per

condition were studied. The selection of annealing temperatures was based on the study [22]. In [22] author claims that ω-phase particles are not dissolved completely at 823 K, whereas the ω-phase is completely dissolved at 843 K.

In the Fig. 7.26. the temperature dependence of the heat flow of samples at different conditions during heating is shown. The first endothermic peak (marked as 1) of non-deformed initial material (blue colour) determines the creation of the ω_{iso} particles. This process starts at around 523 K which is in accordance with [22]. The peak 1 is not visible for non-deformed material annealed up to 823 K (purple colour). This is due to the fact that ω_{iso}-phase particles remain in the material after quenching from 823 K and during consequent heating new particles do not form.
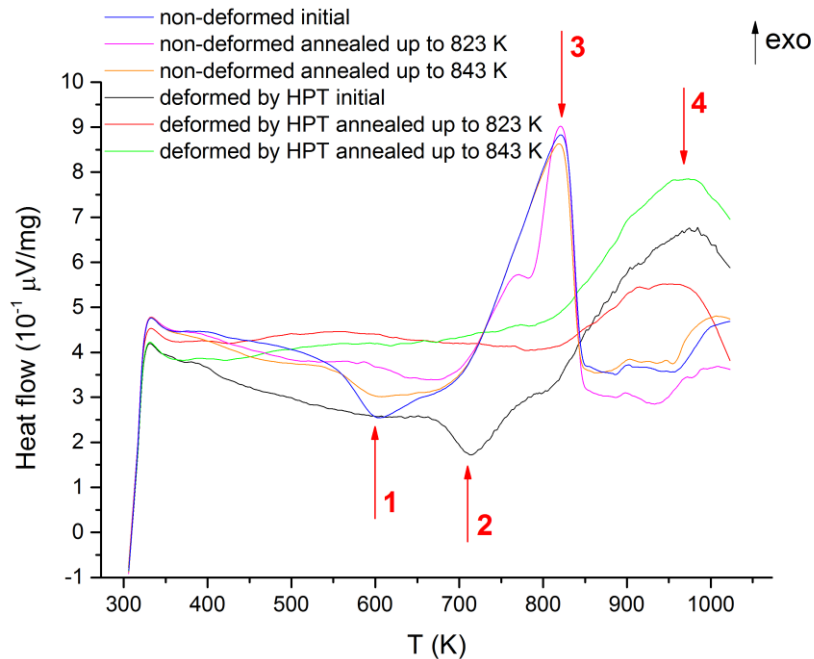
Fig. 7.26. The temperature dependence of the heat flow at the heating rate of 5 5 K/min

However, for non-deformed material annealed up to 843 K (orange colour) an endothermic peak occurs which is consistent with the precipitation of the ω_{iso}-phase particles in the material. The precipitation occurs due to previous annealing up to 843 K after which the ω-phase was dissolved. The growth of ω-phase particles accompanied by the heterogeneous nucleation of α-phase particles starts around 700 K (peak denoted as 3) in the non-deformed material.

62

For material deformed by HPT (no subsequent annealing) the precipitation of the ω-phase particles is probably shifted to higher temperatures (peak marked as 2). This endothermic process for HPT samples is not visible after annealing up to 823 K and 843 K, respectively, which suggests that annealing up to these temperatures may not be sufficient for ω-phase particles dissolution in highly deformed material. Peak denoted as 4 most probably indicates precipitation of the α-phase particles for deformed material by HPT. This exothermic process is also shifted to higher temperatures when compared to non-deformed material. The fact that the α-phase particles are created at higher temperatures in deformed material can have several possible explanations. The first is that energy barrier for nucleation of α-phase particles is higher and the critical radius of α-phase nucleus is not achieved. The second is that if phase transformation is controlled by movement of interface, then the defects in the material may block the movement of the interface. Moreover, peaks marked as 4 in deformed material are broader which is possibly caused by spanning over larger temperature interval or by kinetics of the phase transformation.

To our knowledge, phenomenon of shifting of peaks in DSC measurement in β-Ti alloys or in materials with UFG microstructure has not been reported yet. We cannot explain exactly the phenomenon of the shift based only on the DSC measurement. The precise explanation requires further investigations such as in-situ measurements of evolution of electric resistivity and detail structural investigations by transmission electron microscopy (TEM). The examination of the broadening of peaks in deformed material also needs further investigation such as DSC measurement with different (higher) heating rates.

8. Conclusions

In the present work, the microstructure evolution, mechanical properties, defect structure and phase transformations of ultra-fine grained (UFG) metastable β-titanium alloys, Ti-15Mo and TIMETAL LCB prepared by high pressure torsion (HPT) were investigated. Mechanical properties were studied by microhardness measurements, the microstructure evolution was examined by scanning electron microscopy and electron backscatter diffraction (EBSD). The defect structure was observed by positron annihilation spectroscopy (PAS) and phase transformations by differential scanning calorimetry (DSC).

The most important results of this investigation can be summarized as follows:

- Microhardness of Ti-15Mo and TIMETAL LCB alloys increases with increasing number of HPT revolutions and also with increasing distance from the centre of the sample. The highest microhardness after HPT exceeds significantly the microhardness for two phase α + β heat-treated material.

- The degree of deformation strengthening, defined by hardenability exponent denotes strain hardening in both cases. TIMETAL LCB alloy demonstrates higher hardenability exponent than Ti-15Mo alloy which means that ability of deformation strengthening of the TIMETAL LCB alloy saturates for higher strains.

- Increasingly deformed microstructure was also demonstrated by scanning electron microscopy. In Ti-15Mo alloy, the microstructure is more fragmented than in TIMETAL LCB alloy.

- Twinning-induced grain refinement in Ti-15Mo alloy was demonstrated by electron back-scattered diffraction (EBSD). It was proven that the twinning system {1 1 2} <111> is active during HPT. To our knowledge, twinning-induced grain refinement has not been investigated in β-Ti alloys before.

- Defect structure of the Ti-15Mo alloy was studied by positron annihilation spectroscopy. Dislocation component was the only defect related component in the positron annihilation spectrum. Increasing density of dislocations with increasing strain is in accordance with the microhardness increase.

- Effect of the ultra-fine grained microstructure on the phase transformations was investigated by differential scanning calorimetry (DSC). The

precipitation of the α-phase is shifted to higher temperatures in UFG material. The underlying mechanism cannot be clarified just only on the basis of the DSC measurement. Further measurements must be carried out for an explanation of the effect of UFG microstructure on the phase transformations in metastable β-Ti alloys.

Further work

As it was mentioned before, the effect of the ultra-fine grained microstructure on the phase transformations in the material has to be investigated in details. This study will include in-situ electrical resistivity measurements which is more sensitive to the phase transformations than DSC measurement, especially to formation and dissolution of the ω-phase particles. Based on these measurements the temperature range of the phase transformations can be determined. Pre-annealed samples will be studied by ex-situ transmission electron microscopy and by x-ray diffraction analysis. The most comprehensive study will be carried out by in-situ transmission electron microscopy. During in-situ TEM, nucleation and precipitation of phases should be observed directly.

Furthermore, β-Ti alloys prepared by different severe plastic deformation technique, such as equal-channel angular pressing (ECAP) will be investigated. The observations of the mechanical properties of the material will include microhardness measurement and tensile tests. The advantage of ECAP is bigger size of samples when compared to very small samples prepared by HPT, which allows carrying out the tensile tests. Moreover, the materials strengthening after different techniques of SPD should be compared by microhardness measurement. The defect structure and wide range of experimental techniques allow detail analysis of microstructure, mechanical properties and other physical properties of UFG β-Ti alloys.

Bibliography

[1] C. LEYENS and M. PETERS. *Titanium and titanium alloys*. Wiley-VCH. 2003.

[2] G. LÜTJERING and J. C. WILLIAMS. *Titanium*. Springer-Verlag. 2003.

[3] Titanium. *Wikipedia, http://en.wikipedia.org/wiki/Titanium.* 2015.

[4] I. POLMEAR. *Light alloys: from traditional alloys to nanocrystals*. Butterworth-Heinemann. 2006.

[5] G. WELSCH, R. BOYER and E.W. COLLINGS. *Materials Properties Handbook: Titanium Alloys*. ASM International. 1993.

[6] P. J. BANIA. Beta titanium alloys and their role in titanium industry. *JOM Journal of the Minerals, Metals and Materials Society.* 1994, vol. 46, no.7, pp. 16-19.

[7] S. BANERJEE and P: MUKHOPADHYAY. *Phase transformations: examples from titanium and zirconium alloys.* Elsevier Science. 2007.

[8] S. NAG. *PhD thesis: Influence of beta instabilities on the early stages of nucleation and growth of alpha in beta titanium alloys.* The Ohio State University. 2008.

[9] J. C. WILLIAMS. *Critical review: kinetics and phase transformations*. Titanium Science and Technology. 1973.

[10] T. W. DUREIG, G. T. TERLINDE and J. C. WILLIAMS. *The omega phase reaction in titanium alloys.* Titanium ´80: Science and Technology. 1980, vol.2, pp. 1299-1305.

[11] S. K. SIKKA, Y. K. VOHRA, R. CHIDAMBARAM. *Omega phase in materials.* Progress in Material Science. 2002, vol. 27, pp.245-310.

[12] Y. A. BAGARYATSKIY, T. V. TAGUNOVA and G. I. NOSOVA. *Problemy metallovedeniya i fiziki metalloy (Problems of metallography and metal physics).* Metallurgizdat. 1958, vol. 5.

[13] F. R. BROTZEN, E. L. HARMON Jr. And A. R. TROIANO. *Decomposition of beta titanium.* Journal of Metals. 1955, vol.7.

[14] J. M. SILCOCK, M. H. DAVIES and M. K. HARDY. *The mechanism of phase transformations in solids.* A Symposium, Monograph and Report Series. 1956, vol. 18, pp.93.

[15] Y. A. BAGARYATSKIY, G. I. NOSOVA and T. V. TAGUNOVA. *The crystallographic structure and nature of the omega phae in titanium alloys with chromium*. Doklady Akademii Nauk SSSR. 1955, vol.32, pp. 1225-1228.

[16] E. W. COLLINGS. *The physical metallurgy of titanium alloys*. American Society for Metals. 1984.

[17] D. DE FONTAINE, N. E. PATON and J. C. WILLIAMS. *The omega phase transformation in titanium alloys as an example of displacement controlled reactions*. Acta Metallurgica. 1971, vol. 19, pp. 1153-1162.

[18] D. DE FONTAINE. *Simple models for the omega phase transformation*. Metallurgical and Materials Transactions A. 1988, vol. 19, no. 2, pp. 169-175.

[19] W. G. BURGERS. *On the process of transition of the cubic-body-centered modification into the hexagonal-close-packed modification of zirconium*. Physica. 1934, vol. 1, pp. 561-586.

[20] T. FURUHARA, T. MAKINO, Y. IDEI, H. ISHIGAKI, A. TAKADA and T. MAKI. *Morphology and crystallography of precipitates in Ti-Mo binary alloys*. Materials Transactions, JIM. 1998, vol. 39, pp. 31-39.

[21] T. W. DUERIG, G. T. TERLINDE and J. C. WILLIAMS. *Phase transformations and tensile properties of Ti-10V-2Fe-3Al*. Metallurgical and Materials Transactions A. 1980, vol. 11, no. 12, p. 1987-1998.

[22] P. ZHÁŇAL. *Master thesis: Study of phase transformations in Ti alloys*. Charles University in Prague. 2014.

[23] J. C. WILLIAMS and M. J. BLACKBURN. *The influence of misfit on the morphology and stability of the omega phase in titanium-transition metal alloys*. Transactions of the Metallurgical Society of AIME. 1969, vol. 245.

[24] S. AZIMZADEH and H. J. RACK. *Phase transformations in Ti-6.8Mo-4.5Fe-1.5Al*. Metallurgical and Material Transactions A. 1998, vol. 29, no. 10, pp. 2455-2467.

[25] T. G. LANGDON. *Twenty-five years of ultrafine-grained materials: Achieving exceptional properties through grain refinement*. Acta Materialia. 2013, vol. 61, pp. 7035-7059.

[26] E. O. HALL. *The deformation and ageing of mild steel*. Proceedings of Royal Society of London B. 1951, vol. 64, pp. 747.

[27] N. J. PETCH. *The cleavage strength of polycrystals*. Journal of Iron and Steel Institute 1953, vol. 174, pp. 25.

[28] Y. T. ZHU. *Performance and applications of nanostructured materials produced by severe plastic deformation*. Scripta Materialia. 2004, vol. 51, pp. 825-830.

[29] Y. HUANG and T. G. LANGDON. *Advances in ultrafine-grained materials*. Materials Today. 2013, vol. 16, no. 3, pp. 85-93.

[30] V. M. SEGAL, V. I. REZNIKOV, A. D. DROBYSHEVSKY and V. I. KOPYLOV. *Plastic working of metals by simple shear*. Russian Metallurgy. 1981, vol. 1, pp. 99.

[31] N. A. SMIRNOVA, V. I. LEVIT, V. I. PILYUGIN, R. I. KUZNETSOV, L. S. DAVYDOVA and V. A. SAZONOVA. *Evolution of the structure of FCC single crystals subjected to strong plastic deformation*. Fiz. Metal Metalloved. 1986, vol. 61, pp. 1170.

[32] N. TSUJI, Y. SAITO, H. UTSUNOMIYA and S. TANIGAWA. *Ultra-fine grained bulk steel produced by accumulative roll bonding (ARB) process*. Scripta Materialia. 1999, vol. 40, pp. 795-800.

[33] V. V. STOLYAROV, Y. T. ZHU, T. C. LOWE, R. K. ISLAMGALIEV and R. Z. VALIEV. *A two-step SPD processing of ultrafine-grained titanium*. NanoStructured Materials. 1999, vol. 11, pp. 947-954.

[34] R. K. ISLAMGALIEV, V. I. KAZYHANOV, L. I. SHESTAKOVA, A. V. SHARAFUTDINOV and R. Z. VALIEV. *Microstructure and mechanical properties of titanium (Grade 4) processed by high-pressure torsion*. Materials Science and Engineering A. 2008, vol. 493, pp. 190-194.

[35] V. V. STOLYAROV, Y. T. ZHU, T. C. LOWE and R. Z. VALIEV. *Microstructure and properties of pure Ti processed by ECAP and cold extrusion*. Materials Science and Engineering A. 2001, vol. 303, pp. 82-89.

[36] I. P SEMENOVA, G. I. RAAB, L. R. SAITOVA and R. Z. VALIEV. *The effect of equal-channel angular pressing on the structure and mechanical behavior of Ti-6Al-4V alloy*. Materials Science and Engineering A. 2004, vol. 387-389, pp. 805-808.

[37] M. V. DEGTYAREV, T. I. CHASHCHUKHINA. L. M. VORONOVA, A. M. PATSELOV and V. P. PILYUGIN. *Influence of the relaxation processes on the structure formation in pure metals and alloys under high-pressure deformation*. Acta Materialia. 2007, vol. 55, pp. 6039-6050.

[38] R. Z. VALIEV, YU. V. IVANISENKO, E. F. RAUCH and B. BAUDELET. *Structure and deformation behaviour of Armco iron subjected to severe plastic deformation.* Acta Materialia. 1996, vol. 44, pp. 4705-4712.

[39] A. P. ZHILYAEV and T. G. LANGDON. *Using high-pressure torsion for metal processing: fundamentals and applications.* Progress in Materials Science. 2008, vol. 53, pp. 893-979.

[40] Y. SONG, E. Y. YOON, D. J. LEE, J. H. LEE and H. S. KIM. *Mechanical properties of copper after compression stage of high-pressure torsion.* Materials Science and Engineering A. 2011, vol. 528, pp. 4840-4844.

[41] A. A. POPOV, I. YU. PYSHMINTSEY, S. L. DEMAKOV, A. G. ILLARIONOV, T. C. LOWE, A. V. SERGEYEVA and R. Z. VALIEV. *Structural and mechanical properties of nanocrystalline titanium processed by severe plastic deformation.* Scripta Materialia. 1997, vol. 37, pp. 1089-1094.

[42] R. Z. VALIEV, I. P. SEMENOVA, V. V. LATYSH, H. RACK, T. C. LOWE, J. PETRUZELKA, L. DLUHOS, D. HRUSAK and J. SOCHOVA. *Nanostructured titanium for biomedical applications.* Advanced Engineering Materials. 2009, vol. 10, pp. B15-B17.

[43] Z. B. ZHANG, Y. L. HAO, S. J. LI and R. YANG. *Fatigue behaviour of ultrafine-grained Ti-24Nb-4Zr-8Sn multifunctional biomedical titanium alloy.* Materials Science and Engineering A. 2013, vol. 577, pp. 225-233.

[44] D. KENT, G. WANG, Z. YU, X. MA and M. DARGUSCH. *Strength enhancement of a biomedical titanium alloy through modified accumulative roll bonding technique.* Journal of the Mechanical Behaviour of Biomedical Materials. 2011, vol. 4, pp. 405-416.

[45] T. LI, D. KENT, G. SHA, M. DARGUSCH and J. M. CAIRNEY. *Precipitation of the α-phase in an ultrafine grained beta-titanium alloy processed by severe plastic deformation.* Materials Science and Engineering A. 2014, vol. 605, pp. 144-150.

[46] D. KENT, W. L. XIAO, G. WANG, Z. YU and M. S. DARGUSCH. *Thermal stability of an ultrafine grain β-Ti alloy.* Materials Science and Engineering A. 2012, vol. 556, pp. 582-587.

[47] K. VÁCLAVOVÁ. *Bachelor thesis: Experimental characterization of ultrafine-grained Ti alloys for biomedical use.* Charles University in Prague. 2013.

[48] I. WEISS and S. L- SEMIATIN. *Thermomechanical processing of beta titanium alloys – an overview.* Materials Science and Engineering A. 1998, vol. 243, pp. 46-65.

[49] G. GOTTSTEIN. *Physical foundations of Materials Science.* Springer-Verlag. 2004.

[50] S. V ZHEREBTSOV, G. S. DYAKONOV, A. A. SALEM, S. P. MALYSHEVA, G. A. SALISHCHEV and S. L. SEMIATIN. *Evolution of grain and subgrain structure during cold rolling of commercial-purity titanium.* Materials Science and Engineering A. 2011, vol. 528, pp. 3474-3479.

[51] D. H. HONG and S. K. HWANG. *Microstructural refinement of CP-Ti by cryogenic channel-die compression involving mechanical twinning.* Materials Science and Engineering A. 2012, vol. 555, pp. 106-116.

[52] C. S. MEREDITH and A.S. KHAN. *The microstructural evolution and thermo-mechanical behaviour of UFG Ti processed via equal channel angular pressing.* Journal of Materials Processing Technology. 2015, vol. 219, pp. 257-270.

[53] *Supplier technical sheet.* Carpenter Co. Belgium. 2012.

[54] J. DISEGI. *Implant Materials. Wrought Titanium -15 % Molybdenum.* Synthes. 2009.

[55] ASTM Standard F 2066. *Standard specification for wrought titanium-15Molybdenum for surgical implant applications.* ASTM International, West Conshohocken, PA.

[56] M. JANEČEK, J. ČÍŽEK, J. STRÁSKÝ, K. VÁCLAVOVÁ, P. HRUŠKA, V. POLYAKOVA, S. GATINA and I. SEMENOVA. *Microstructure evolution in solution treated Ti15Mo alloy processed by high pressure torsion.* Materials Characterization. 2014, vol. 98, pp. 233-240.

[57] J. ŠMILAUEROVÁ. *Master thesis: Phase transformations and microstructure changes in TIMET LCB alloy.* Charles University in Prague. 2012.

[58] Y. KOSAKA, S. P. FOX, K. FALLER and S. H. REICHMAN. *Properties and processing of TIMETAL LCB.* Journal of Materials Engineering and Performance. 2005, vol. 14, pp. 792-798.

[59] B. KOKUOZ. *Master thesis: The role of crystallographic relationships between alpha and beta phases on the elevated temperature isothermal phase transformation kinetics in TIMETAL LCB (Ti-6.5Mo-4.5Fe-1.5Al).* Clemson University. 2008.

[60] Vickers hardness test. *Wikipedia, http://en.wikipedia.org/wiki/Vickers_hardness_test.* 2015.

[61] W. WERNER. *Interaction of electron beams with matter.* 2012.

[62] A. J. WILKINSON and P. B. HIRSCH. *Electron diffraction based techniques in scanning electron microscopy of bulk materials.* Micron. 1997, vol. 28, pp. 279-308.

[63] J. I. GOLSTEIN, D. E. NEWBURY, P. ECHLIN, D. C. JOY, C. E. LYMAN and E. LIFSHIN. *Scanning electron microscopy and X-ray microanalysis*, Kluwer Academic/Plenum Publish. 2003.

[64] Energy-dispersive X-ray spectroscopy. *Wikipedia, http://en.wikipedia.org/wiki/Energy-dispersive_X-ray_spectroscopy.* 2015.

[65] New Facility a Positive for Positron Spectroscopy Advances. *http://www.wpafb.af.mil/news/story.asp?id=123193286.* 2010.

[66] R.N. WEST. *Positron studies of lattice defects in metals*. in: P. Hautojärvi (Ed.), Positrons in Solids, Springer-Verlag, Berlin, 1979.

[67] J. ČÍŽEK. *Defect studies by positron annihilation*, *http://physics.mff.cuni.cz/kfnt/vyuka/anihilace/prednaska8.pdf.* 2013.

[68] B. BARBIELLINI, P. GENOUD and T. JARLBORG. *Calculation of positron lifetimes in bulk materials*. Journal of Physics: Condensed Matter. 1991. Vol. 3, pp. 7631-7640.

[69] J.M.C. ROBLES, E. OGANDO and F. PLAZAOLA. *Positron lifetime calculation for the elements of the periodic table*. Journal of Physics: Condensed Matter. 2007, vol. 19, pp. 176-222.

[70] I. PROCHAZKA, J. CIZEK, G. BRAUER and W. ANWAND. *Slow-positron implantation spectroscopy in nanoscience.* Nanocon 2009.

[71] P. HAUTOJÄRVI, C. CORBEL. In: Dupasquier A, Mills AP (eds) Proceedings of the International School of Physics „Enrico Fermi", Course CXXV, IOS Press, Varena, 1995, p.491.

[72] F. BEČVÁŘ, J. ČÍŽEK, L. LESTÁK, I. NOVOTNY , I. PROCHÁZKA and F. ŠEBESTA. *A high-resolution BaF2 positron-lifetime spectrometer and experience with its long-term exploitation*. Nuclear Instruments and Methods in Physics Research Section A: Accelerators, Spectrometers, Detectors and Associated Equipment. 2000, vol. 443, no. 2-3, pp. 557–577.

[73] M. KAWASAKI, H-J. LEE, B. AHN, A. P. ZHILYAEV and T. G. LANGDON. *Evolution of hardness in ultrafine-grained metals processed by high-pressure torsion.* Journal of Materials Research and Technology. 2014, vol. 3, pp. 311-318.

[74] K. EDALATI and Z. HORITA. *Universal Plot for Hardness Variation in Pure Metals Processed by High-Pressure Torsion.* Materials Transactions. 2010, vol. 51, pp. 1051-1054.

[75] Y. C. WANG and T. G. LANGDON. *Effect of heat treatment on microstructure and microhardness evolution in a Ti-6Al-4V alloy processed by high pressure torsion.* Journal of Materials Science. 2013, vol. 48, pp. 4646-4652.

[76] H-J. LEE, B. AHN, M. KAWASAKI and T. G. LANGDON. *Evolution in hardness and microstructure of ZK60A magnesium alloy processed by high-pressure torsion.* Journal of Materials Research and Technology. 2015, vol. 4, pp- 18-25.

[77] H. PAXTON. *Experimental verification of the twin system in alpha-iron.* Acta Metallurgica. 1953, vol. 1., pp. 141-143.

[78] J. W. CHRISTIAN and S. MAHAJAN. *Deformation twinning and its effect on crack extension.* Progress in Materials Science 1995, vol. 39., pp. 1-157.

[79] Y. WANG, A. HODGE, J. BIENER, A. HAMZA, D. BARNES, K. LIU and T. NIEH. *Deformation twinning during nanoindentation of nanocrystalline Ta.* Applied Physics Letters. 2005, vol. 86.

[80] Y. YANG, S. WU, G. LI, Y. LI, Y. LU, K. YANG and P. GE. *Evolution of deformation mechanisms of Ti–22.4Nb–0.73Ta–2Zr–1.34O alloy during straining.* Acta Materialia. 2010, vol. 58., pp. 2778-2787.

[81] Y. YANG, G. P. LI, H. WANG, S. Q. WU, L. C. ZHANG, Y. L. LI and K. YANG. *Formation of zigzag-shaped {1 1 2} 〈1 1 1〉 β mechanical twins in Ti-24.5Nb-0.7Ta-2Zr-1.4O alloy.* Scripta Materialia. 2012, vol. 66., pp. 211-214.

[82] L. LI, W. MEI, H. XING, X. L. WANG and J. SUN. *Zigzag configuration of mechanical twin and stress-induced omega phase in metastable β Ti-34Nb (at%) alloy.* Journal of Alloys and Compounds. 2015, vol. 625, pp. 188-192.

[83] X. H. MIN, K. TSUZAKI, S. EMURA, T. SAWAGUCHI, S. II and K. TSUCHIYA. *{3 3 2} 〈1 1 3〉 Twinning system selection on a β-type Ti-15Mo-5Zr polycrystalline alloy.* Materials Science and Engineering A. 2013, vol. 579, pp. 164-169.

[84] X. H MIN, K. TSUZAKI, S. EMURA and K. TSUCHIYA. *Heterogeneous twin formation and its effect on tensile properties in Ti-Mo based β titanium alloys.* Materials Science and Engineering A. 2012, vol. 554, pp. 53-60.

[85] E. BERTRAND, P. CASTANY, I. PÉRON and T. GLORIANT. *Twinning system selection in a metastable β-titanium alloys by Schmid factor analysis.* Scripta Materialia. 2011, vol. 64, pp. 1110-1113.

[86] B. JINAG, K. TSUCHIYA, S. EMURA and X.H. MIN. *Effect of high-pressure torsion process on precipitation behaviour of α phase in β-type Ti–15Mo alloy.* Materials Transactions. 2014, vol. 55, pp. 877–884.

[87] Y. LI, S. WU, H. BIAN, N. TANG, B. LIU, Y. KOIZUMI and A. CHIBA. *Grain refinement due to complex twin formation in rapid hot forging of magnesium alloy.* Scripta Materialia. 2013, vol. 63, pp.171-174.

[88] H. MIURA, M. ITO, X. YANG and J. J. JONAS. *Mechanisms of grain refinement in Mg–6Al–1Zn alloy during hot deformation.* Materials Science and Engineering A. 2012, vol. 538, pp. 63-68.

[89] H. W. ZHANG, Z. K. HEI, G. LIU, J. LU and K. LU. *Formation of nanostructured surface layer on AISI 304 stainless steel by means of surface mechanical attrition treatment.* Acta Materialia. 2003, vol. 51., pp. 1871-1881.

[90] K. WANG, N. R. TAO, G. LIU, J. LU and K. LU. *Plastic strain-induced grain refinement at the nanometer scale in copper.* Acta Materialia. 2006, vol. 54, pp. 5281-5291.

[91] Y. J. CHEN, Y. J LI, J. C. WALMSLEY, S. DUMOULIN, S. S. GIREESH, S. ARMADA, P. C. SKARET and H. J. ROVEN. *Quantitative analysis of grain refinement in titanium during equal channel angular pressing.* Scripta Materialia. 2011, vol. 64, pp. 904-907.

[92] L.C. SMEDSKJAER, M. MANNINEN, M.J. FLUSS. *An alternative interpretation of positron annihilation in dislocations.* Journal of Physics F. 1980, vol.10., pp. 2237.

[93] R. Z. VALIEV, R. K. ISLAMGALIEV, I. V. ALEXANDROV. *Bulk nanostructured materials from severe plastic deformation.* Progress in Materials Science. 2000, vol. 45, pp. 103–189.

[94] M. JANEČEK, J. STRÁSKÝ, J. ČÍŽEK, P. HARCUBA, K. VÁCLAVOVÁ, V.V. POLYAKOVA, I.P. SEMENOVA. *Mechanical properties and dislocation structure evolution in Ti6Al7Nb alloy processed by high pressure torsion.* Metallurgical and Materials Transactions A. 2014, vol. 45A, pp. 7 – 15.